An improved methodology to estimate cross-scale kinetic energy transfers from third-order structure functions using regularized least-squares

Manuel O. Gutierrez-Villanueva,[a] Bruce D. Cornuelle,[b] Sarah T. Gille,[b] Matthew R. Mazloff,[b] Dhruv Balwada,[a]

[a] *Lamont-Doherty Earth Observatory, Columbia University, Palisades, NY*

[b] *Scripps Institution of Oceanography, University of California San Diego, La Jolla, CA*

Corresponding author: Manuel O. Gutierrez-Villanueva, mg4864@columbia.edu

ABSTRACT: Several methods exist for estimating cross-scale kinetic energy (KE) transfers; however, most are ill-adapted for sparse ocean observations, hindering the study of oceanic KE transfers. A newly developed third-order structure function, $D3(r)$, framework allows estimation of KE injections $\xi_j(k)$ and spectral flux $F(k)$ across scales using sparse data. This approach requires inverse methods to convert between separation r and wavenumber k space. A previous study employed the structure-function framework to estimate $F(k)$ and $\xi_j(k)$ using non-negative least squares (NNLS), assuming that the spectral flux is an increasing function of wavenumber, an assumption not always satisfied. Here, an improved methodology is presented to estimate $F(k)$ and ξ_j using regularized least-squares (RLS), where the inclusion of prior uncertainty in $D3(r)$ and ξ_j reduces overfitting. Moreover, the improved methodology allows for estimating both positive and negative injections without making assumptions about the shape of the spectral flux. As a proof of concept, the improved methodology was implemented in an eddy-rich quasi-geostrophic simulation output. RLS quantitatively diagnoses the structure of $F(k)$, including both positive and negative $\xi_j(k)$, an aspect unattainable with NNLS. The improved methodology was then applied to data from two drifter experiments in the Gulf of Mexico. The analysis reveals the presence of bidirectional energy transfers, with a KE inverse transfer at mesoscales in both seasons and a forward transfer at submesoscales that is stronger in winter than in summer. Unlike NNLS, RLS fits $D3(r)$ better as the method detects wavenumbers where $\xi_j < 0$ while preserving smoothness. This improved methodology allows for a more refined analysis of KE transfers from sparse observations.

1. Introduction

Cross-scale kinetic energy (KE) transfers play a key role in several aspects of ocean circulation (Ferrari and Wunsch 2009), as they mediate the flow of energy from the scales where it is injected through atmospheric forcing, tides, and solar heating to the scales where it is ultimately dissipated by molecular viscosity. Quasi-geostrophic turbulence theory, a cornerstone of classical ocean dynamics, suggests that at mesoscales, O(50-200) km, energy is transferred on average toward larger scales (inverse cascade), and satellite observations provide strong evidence to support this (Scott and Wang 2005; Vallis 2017). Recently, a new body of numerical and observational work has suggested that energy at submesoscales O(1-10) km may be transferred downscale (forward cascade) en route to dissipation (Schubert et al. 2020; Balwada et al. 2022; Freilich et al. 2023; Tedesco et al. 2024; Naveira Garabato et al. 2022). It has also been suggested that mesoscale and submesoscale flows interact by exchanging energy (Sasaki et al. 2017; Steinberg et al. 2022) and that these interactions may help modulate how oceanic flows redistribute heat, carbon, and other tracers in the global ocean, with important consequences for global climate (Balwada et al. 2021; Zhang et al. 2023).

Several methods exist to study the energy transfer across scales when gridded data from numerical simulations or mapped observations are available. The most commonly used are spectral methods, which have traditionally been used for estimating KE transfers from gridded velocity fields by considering the Fourier transform in wavenumber space (e.g. Capet et al. 2008; Ajayi et al. 2021; Dong et al. 2020). In addition to requiring uniformly gridded data, spectral methods also require that data be preprocessed by removing spatiotemporal means and windowing to minimize edge effects in nonperiodic domains, which can quantitatively and qualitatively impact the estimated transfer (Aluie et al. 2018). Also, the estimated transfers are obtained as bulk or non-local estimates over the entire study domain, and localized details cannot be inferred. Using wavelets instead of Fourier transforms allows local properties to be probed but still entails similar pre-processing (Uchida et al. 2023). More recently, a coarse-graining approach has been introduced in oceanography (Aluie et al. 2018), which parses flow at different scales with the help of filtering (e.g., top-hat filter). This method also relies on gridded data but has the advantage of estimating the cross-scale transfers at each location, similar to wavelets, and avoids the need to artificially impose periodicity (Aluie et al. 2018; Srinivasan et al. 2023; Freilich et al. 2023; Naveira Garabato et al. 2022; Tedesco et al. 2024;

Schubert et al. 2023, 2020; Storer et al. 2023; Yu et al. 2024). Since all these approaches depend on gridded data, they are technically challenging to implement with sparse or non-uniformly sampled observations, impeding their use to study KE transfers in the real ocean.

An alternative to relying on gridded information for estimating KE transfers involves using third-order velocity structure functions. Third-order structure functions are foundational in three-dimensional turbulence theory. In particular, when kinetic energy cascades downscale at a rate of ϵ within the inertial range (i.e., scales away from direct forcing and viscous dissipation), the theory predicts the exact result $\langle \delta u_L^3(r) \rangle = -\frac{4}{5}\epsilon r$, known as Kolmogorov's four-fifths law (Kolmogorov 1991). Here r is the two-point separation distance, δu_L is the longitudinal velocity increment ($\delta u_L^n \equiv (\delta u_L)^n$ indicates the nth power of the increment), and $\langle \cdot \rangle$ denotes an ensemble average. Although this exact law is unlikely to hold in more complex, realistic scenarios, the sign of the third-order structure function has been widely employed as a heuristic tool to infer the direction of energy transfer in studies of natural flows (Lindborg 1999; Lindborg and Cho 2001; Cho and Lindborg 2001; Qiu et al. 2022; Balwada et al. 2016; Poje et al. 2017). However, this heuristic approach faces limitations due to challenges in identifying inertial ranges in oceanic flows and determining the turbulence regime (e.g., 2D, 3D, or quasi-geostrophic). These uncertainties undermine the robustness of ϵ estimates when the underlying assumptions are violated.

A recently developed framework by Xie and Bühler (2019) employs third-order structure functions to estimate the energy injection rates across multiple forcing scales and the spectral flux. The new framework does not require identifying inertial ranges and can be applied to scattered and heterogeneous data under assumptions of axisymmetry (isotropy) and homogeneity. Balwada et al. (2022) implemented this methodology using a piecewise function for the spectral flux to estimate the structure of KE transfers in spectral space, using two drifter datasets collected in summer and winter that resolve submesoscale flows down to $O(100)$ m. They employed a non-negative least-squares (NNLS) method to invert the third-order structure functions and estimate KE injection rates and spectral flux. However, the NNLS method inherently cannot capture negative KE injection rates (indicative of KE transfer convergence in spectral space). As a result, the derived KE transfers are strictly increasing with wavenumber, an assumption that may not hold universally, such as during the conversion of KE to potential energy.

Here, we improve on the estimation of the KE transfers presented by Balwada et al. (2022) by utilizing regularized least-squares (RLS) (e.g. Wunsch 1996; Kachelein et al. 2022). The RLS approach allows us to 1) prescribe a prior uncertainty in the KE injection rates, reducing overfitting in the inversion problem that leads to non-physical energy transfers when using ordinary least-squares, 2) propagate the uncertainty in the estimated third-order structure functions to the calculated KE transfers and injection rates, 3) make no assumptions regarding the direction of the KE transfers, and thus 4) potentially identify energy sinks.

To demonstrate the success of RLS in estimating KE transfers, we first use an idealized two-layer quasi-geostrophic (QG) model that generates mesoscale eddies. In this scenario, energy is injected into the flow, transferred to the larger-scale flows, and dissipated at larger scales through bottom drag. We show that the RLS method resolves the expected shape of the KE transfers as it resolves KE sinks (negative KE injection density per wavenumber) that are otherwise unresolved by the NNLS method, as the latter is incapable of estimating negative injection rates. We then apply this methodology to drifter data from two targeted experiments in the Gulf of Mexico (Balwada et al. 2022), improving the estimates of the bidirectional transfers and its seasonality. The results confirm an inverse transfer at mesoscales and a forward transfer at submesoscales, modulated by seasonal energy injection. Unlike NNLS, RLS fits the estimated third-order structure function better, as it captures KE sinks. The paper is organized as follows: Section 2 reviews the structure-function and KE transfer theory. The improved methodology is explained in Section 3. Details of the QG model setup, the drifter data, and the steps to estimate structure functions are presented in Section 4. Results from the QG model are presented in Section 5a, while Section 5b explores drifter experiments and compares estimates with prior studies. Also, Section 5 presents sample distributions of the third-order structure function, along with the steps taken to estimate prior uncertainties in both the structure function and injection rates. Section 6 concludes with a summary of the improved methodology's results, advantages, and limitations.

2. Structure Function Framework

Structure functions provide a powerful framework for diagnosing ocean energetics from sparse observations. The foundation of this approach is the estimation of two-point differences in scalars

or vectors, such as velocity differences:

$$\delta\mathbf{u}(\mathbf{s},\mathbf{r},t) = \mathbf{u}(\mathbf{s}+\mathbf{r},t) - \mathbf{u}(\mathbf{s},t), \tag{1}$$

where $\delta\mathbf{u}$ represents the velocity difference between two points $\mathbf{s}$ and $\mathbf{s}+\mathbf{r}$ separated by the vector $\mathbf{r}$ at time t. These velocity differences are the central focus of this study. To avoid reliance on fixed geographical coordinates, we decompose $\delta\mathbf{u}$ into longitudinal and transverse components $\delta\mathbf{u} = (\delta u_L, \delta u_T)$:

$$\delta u_L = \delta\mathbf{u}\cdot\frac{\mathbf{r}}{|\mathbf{r}|}, \quad \delta u_T = \frac{\widehat{\mathbf{z}}\cdot(\delta\mathbf{u}\times\mathbf{r})}{|\mathbf{r}|}, \tag{2}$$

where $\widehat{\mathbf{z}}$ is the vertical unit vector.

a. First- and second-order velocity structure functions

Given a sample set of velocity differences across many random pairs, velocity structure functions are defined as raw statistical moments of these random variables. Here we define the first-order structure function $D1(r)$ for stationary, homogeneous and isotropic flows as:

$$D1(r) = D1_L(r) + D1_T(r) = \langle\delta u_L(\mathbf{s},\mathbf{r},t)\rangle + \langle\delta u_T(\mathbf{s},\mathbf{r},t)\rangle, \tag{3}$$

where $r = |\mathbf{r}|$, and $\langle\cdot\rangle$ represents the ensemble average over all members of the ensemble at each r. Often, in practice, and when the assumptions of stationarity, isotropy, and homogeneity approximately hold, ensemble averaging is replaced by averaging over all samples corresponding to a spatio-temporal average. Also, we choose to define $D1(r)$ as a sum of the longitudinal $D1_L(r)$ and transverse $D1_T(r)$ components, but other choices with different interpretations are also valid. $D1(r)$ provides a measure of the strength of the gradients in the mean flow and is rarely discussed in the theoretical literature that often assumes that the background mean flow is zero or constant.

Similarly, the second-order structure is defined as,

$$D2(r) = D2_{LL}(r) + D2_{TT}(r) = \langle\delta u_L^2(\mathbf{s},\mathbf{r},t)\rangle + \langle\delta u_T^2(\mathbf{s},\mathbf{r},t)\rangle, \tag{4}$$

which is a sum of the longitudinal and transverse components, denoted as $D2_{LL}(r)$ and $D2_{TT}(r)$, respectively. $D2(r)$ provides a measure of the energy within the isotropic, stationary 2D flow at a

scale r and can be precisely connected to the isotropic KE spectrum $E(k)$ as:

$$D2(r) = 2\int_0^\infty E(k)[1 - J_0(kr)]dk, \tag{5}$$

where J_0 is the zeroth-order Bessel function (Bennett 1984), $k = \sqrt{k_x^2 + k_y^2}$ is the isotropic wavenumber (k_x and k_y are the zonal and meridional wavenumbers, respectively), and dk is the wavenumber resolution. Assuming the existence of a KE spectrum that follows a power law $E(k) \sim k^{-\theta}$, one can show using (5) that the second-order structure function has a form of $D2(r) \sim r^{\theta-1}$ where θ is the wavenumber spectral slope (Bennett 1984).

b. Third-order structure function and cross-scale KE transfers

At the third order, we follow Balwada et al. (2022), employing the theoretical framework of Xie and Bühler (2019), who derived a formulation (from the Karman–Howarth–Monin equation) capable of capturing bidirectional KE transfers by using the calculated isotropic third-order structure function. The longitudinal component of the third-order structure function is defined as

$$D3(r) = D3_{LLL}(r) + D3_{LTT}(r) = \langle \delta u_L(\mathbf{s},\mathbf{r},t)[\delta u_L^2(\mathbf{s},\mathbf{r},t) + \delta u_T^2(\mathbf{s},\mathbf{r},t)]\rangle. \tag{6}$$

$D3(r)$ is related to azimuthally averaged 2D cross-scale KE transfers $F(k)$ through the following relationship (i.e., a Hankel transform):

$$D3(r) = -4r\int_0^\infty \frac{1}{k}F(k)J_2(kr)dk, \tag{7}$$

where J_2 is the second-order Bessel function (Xie and Bühler 2019). $F(k) > 0$ indicates a forward transfer (i.e., KE transfer toward smaller scales); conversely, $F(k) < 0$ indicates an inverse transfer (toward larger scales). Under the assumptions of periodicity, isotropy, and homogeneity, the spectral transfers are obtained from the KE equation as (e.g., Ajayi et al. 2021; Capet et al. 2008; Dong et al. 2020):

$$F_\Pi(k) = -\int_k^{k_{max}} \mathrm{Re}\left[\widehat{\mathbf{u}}^* \cdot \widehat{(\mathbf{u}\cdot\nabla\mathbf{u})}\right]dk, \tag{8}$$

where $\widehat{()}$ indicates Fourier transform, $()^*$ is the complex conjugate, and $\nabla_H = (\partial_x, \partial_y)$ is the horizontal velocity gradient operator.

Xie and Bühler (2019) considered an idealized, single forcing scale scenario k_f with spectral transfer:

$$F(k) = -\epsilon_u + \epsilon H(k - k_f), \tag{9}$$

where $\epsilon_u > 0$ is the upscale energy transfer (i.e., upscale KE injection rate), $\epsilon = \epsilon_u + \epsilon_d$ is the total energy input rate ($\epsilon_d > 0$ represents the downscale transfer), H is the Heaviside function, and k_f is the forcing scale. This form captures bidirectional energy transfers and assumes that dissipation occurs at $k \to 0$ and $k \to \infty$ (see Fig. 1 in Xie and Bühler 2019, for possible shapes (9) can resolve).

The generalized expression of $F(k)$ for multiple scales is (Balwada et al. 2022)

$$F(k) = -\overline{\epsilon} + \sum_{j=1}^{N_k} \xi_j H(k - k_j)\, dk_j, \tag{10}$$

where $\overline{\epsilon}$ is the KE transfer rate at wavenumbers $k < k_1$ (with k_1 defined to be the smallest resolved wavenumber), ξ_j is the KE injection density (i.e., KE injection rate per wavenumber) at each wavenumber k_j, and N_k is the number of chosen wavenumbers. The term $\overline{\epsilon}$ complements ϵ_u from (9), and may be positive for upscale transfer or negative for downscale transfer at $k < k_1$. Substituting (10) in (7) yields

$$D3(r) = 2\overline{\epsilon} r - \sum_{j=1}^{N_k} 4 \frac{\xi_j}{k_j} J_1(k_j r) dk_j. \tag{11}$$

This equation provides the starting point for a discrete linear inverse problem, where the goal is to estimate $\overline{\epsilon}$ and ξ_j at a selected range of k_j from an estimated $D3(r)$. By accommodating multiple forcing scales k_j and allowing for a general form of $F(k)$, (11) overcomes the limitations of, for example, Kolmogorov's (1991) law, which applies only to inertial ranges with unidirectional transfers (see Xie and Bühler 2019, for details).

Balwada et al. (2022), using the generalized expression (10) of $F(k)$, constrained the KE injection density ξ_j at each forcing scale to be positive $\xi_j > 0$, so $F(k)$ was treated as an increasing function

of k. In the ocean, nonetheless, KE can be injected and/or lost at different scales, breaking the assumption of only positive injection made by Balwada et al. (2022). Here, we relax this assumption and allow for the energy injection density at each k_j to take either sign: $\xi_j > 0$ indicates local KE injection (divergence of KE transfer $F(k)$) at k_j, and $\xi_j < 0$ indicates energy sink (convergence), so spectral transfers $F(k)$ have no specific behavior.

The following section describes the inverse problem and the RLS fitting employed to estimate the KE injections and the spectral flux.

3. Regularized Least Squares

We use a least-squares approach to solve the linear problem, writing (11) as a matrix equation:

$$\mathbf{y} = \mathbf{H}\mathbf{x} + \mathbf{e}, \tag{12}$$

where $\mathbf{x}$ is the column vector of size $M \times 1$ (where $M = N_k + 1$) representing the unknown parameters ($\overline{\epsilon}$ and ξ_j), $\mathbf{y}$ is the vector of data to fit (i.e., $D3(r)$) of size $N_r \times 1$ ($N(r)$ is the number of discrete r bins), $\mathbf{e}$ is the residual, and $\mathbf{H}$ is the model matrix formulated from (11) of size $N_r \times M$ defined as:

$$\mathbf{H} = \begin{bmatrix} 2r_1 & -4\frac{dk}{k_1}J_1(r_1k_1) & -4\frac{dk}{k_2}J_1(r_1k_2) & -4\frac{dk}{k_3}J_1(r_1k_3) & \cdots & -4\frac{dk}{k_{N_k}}J_1(r_1k_{N_k}) \\ 2r_2 & -4\frac{dk}{k_1}J_1(r_2k_1) & -4\frac{dk}{k_2}J_1(r_2k_2) & -4\frac{dk}{k_3}J_1(r_2k_3) & \cdots & -4\frac{dk}{k_{N_k}}J_1(r_2k_{N_k}) \\ 2r_3 & -4\frac{dk}{k_1}J_1(r_3k_1) & -4\frac{dk}{k_2}J_1(r_3k_2) & -4\frac{dk}{k_3}J_1(r_3k_3) & \cdots & -4\frac{dk}{k_{N_k}}J_1(r_3k_{N_k}) \\ \vdots & \vdots & \vdots & \vdots & \ddots & \vdots \\ 2r_{N_r} & -4\frac{dk}{k_1}J_1(r_{N_r}k_1) & -4\frac{dk}{k_2}J_1(r_{N_r}k_2) & -4\frac{dk}{k_3}J_1(r_{N_r}k_3) & \cdots & -4\frac{dk}{k_{N_k}}J_1(r_{N_r}k_{N_k}) \end{bmatrix}, \tag{13}$$

where k_{N_k} is the Nyquist wavenumber, r_{N_r} is the largest separation scale resolved, and dk_j is the wavenumber spacing.

The ordinary least-squares method is ill-suited for inverting (11) since the method can overfit data as the size of the fitted parameters is unconstrained when minimizing the mean square error $\mathbf{e}^2 = ||\mathbf{H}\mathbf{x} - \mathbf{y}||_2^2$, even when weighted using the data's prior uncertainty. Consequently, ordinary least-squares methods tend to capture all the variability at the resolved scales rather than the broader patterns, producing non-physical KE injections and transfers with limited physical insight (see Supplementary Information F.2 in Balwada et al. 2022). To overcome this limitation, Balwada

et al. (2022) constrained their least-squares method by assuming that energy injection rates ξ_j were always non-negative, which is equivalent to assuming that $F(k)$ is purely an increasing function of k.

RLS fitting i) permits the identification of convergence of KE transfers ($\xi_j < 0$), ii) assumes no specific direction of the spectral flux $F(k)$, and iii) propagates the uncertainty of the fitted parameters ξ_j and $\overline{\epsilon}$ and data $D3(r)$ to the calculated $F(k)$. An advantage of RLS is that it reduces overfitting (with some bias in our estimated parameters) by choosing a constraint with prior knowledge of the expected values. Additionally, RLS fitting is applicable for both under-determined and over-determined systems. RLS assumes that the terms in (12), $\mathbf{x}$ and $\mathbf{e}$ (thus, the samples of $D3(r)$), have Gaussian distributions. This assumption does not preclude the use of RLS when errors deviate from Gaussianity, as the solution remains unchanged, though the posterior uncertainty estimates may no longer be appropriate. Accounting for non-Gaussian error distributions would require an alternative to RLS, which, to our knowledge, remains to be explored.

If these distributions are Gaussian, then following Kachelein et al. (2022) and Wunsch (1996), the most probable model solution is given by

$$\widetilde{\mathbf{x}} = \left(\mathbf{H}^{\mathrm{T}}\mathbf{W}^{-1}\mathbf{H} + \mathbf{P}^{-1}\right)^{-1}\mathbf{H}^{\mathrm{T}}\mathbf{W}^{-1}\mathbf{y}, \tag{14}$$

where $\mathbf{W} = \langle \mathbf{e}\mathbf{e}^{\mathrm{T}} \rangle$ is the data covariance matrix representing the prior data uncertainty and is of size $N_r \times N_r$; $\mathbf{P} = \langle \mathbf{x}\mathbf{x}^{\mathrm{T}} \rangle$ is the covariance matrix representing the prior uncertainty of the fitted parameters and is $M \times M$ (Kachelein et al. 2022; Wunsch 1996). In our work, as a practical convenience, $\mathbf{W}$ and $\mathbf{P}$ are defined to be diagonal matrices with off-diagonal entries of zero and with the diagonals set to the squared uncertainty of $D3(r)$ and $\overline{\epsilon}$, and ξ_j, respectively. We can recover the ordinary least-squares solution in (14) by setting the elements on the diagonal of $\mathbf{W}$ to 1 and letting $\mathbf{P}^{-1} \to 0$. The addition of $\mathbf{P}$ in (14) constrains the size of the solution $\mathbf{x}$, preventing it from straying too far from our prior knowledge. This allows for unique solutions even when $\mathbf{H}$ is rank deficient.

We can gain knowledge of the statistics of the differences between the expected true and estimated parameters from the posterior uncertainty covariance matrix

$$\mathbf{C}_{\mathbf{xx}} = \left\langle (\mathbf{x} - \widetilde{\mathbf{x}})(\mathbf{x} - \widetilde{\mathbf{x}})^{\mathrm{T}} \right\rangle = \left(\mathbf{H}^{\mathrm{T}}\mathbf{W}^{-1}\mathbf{H} + \mathbf{P}^{-1}\right)^{-1}, \tag{15}$$

where the diagonal of (15) represents the squared uncertainty of $\overline{\epsilon}$, and ξ_j. The ridge regression equation presented by Wunsch (1996) is analogous to (14). We propagate the uncertainty in ξ_j and $\overline{\epsilon}$ in (15) to uncertainty in transfers $F(k)$ as

$$\mathbf{F_{xx}} = \left\langle (\mathbf{Gx})(\mathbf{Gx})^{\mathrm{T}} \right\rangle = \mathbf{G C_{xx} G}^{\mathrm{T}}, \tag{16}$$

where $\mathbf{G}$ is the $N_k \times M$ transformation matrix formulated with (10):

$$\mathbf{G} = \begin{bmatrix} -1 & H(k_1-k_1)dk & H(k_1-k_2)dk & H(k_1-k_3)dk & \cdots & H(k_1-k_{N_k})dk \\ -1 & H(k_2-k_1)dk & H(k_2-k_2)dk & H(k_2-k_3)dk & \cdots & H(k_2-k_{N_k})dk \\ -1 & H(k_3-k_1)dk & H(k_3-k_2)dk & H(k_3-k_3)dk & \cdots & H(k_3-k_{N_k})dk \\ \vdots & \vdots & \vdots & \vdots & \ddots & \vdots \\ -1 & H(k_{N_k}-k_1)dk & H(k_{N_k}-k_2)dk & H(k_{N_k}-k_3)dk & \cdots & H(k_{N_k}-k_{N_k})dk \end{bmatrix}. \tag{17}$$

The diagonal of $\mathbf{F_{xx}}$ (16) represents the squared uncertainty of $F(k)$, whereas the off-diagonal elements represent correlated uncertainty.

4. Datasets and Methodological Details

In this study, we show that the RLS technique is capable of estimating the shape and magnitude of the KE transfers by applying it to a two-layer QG model output where the dynamics and energetics are known. After demonstrating the utility of the improved methodology, we apply it to drifter observations from two targeted experiments in the Gulf of Mexico. These two datasets and the steps taken to estimate the structure functions are described in this section.

1) Two-layer QG model

An eddy-rich horizontal velocity field (u, v) was simulated using a two-layer QG model (PyQG; Abernathey et al. 2022) (see details in Appendix A) to test whether the RLS methodology can quantify all the details of the spectral transfers.

The model configuration is similar to the high-resolution eddy configuration of Ross et al. (2023), which generates an eddy field (Fig. 1). The configuration is a flat-bottom doubly periodic square domain of size $L_x = L_y = 1000$ km, with $n_x = n_y = 256$ corresponding to a uniform grid spacing

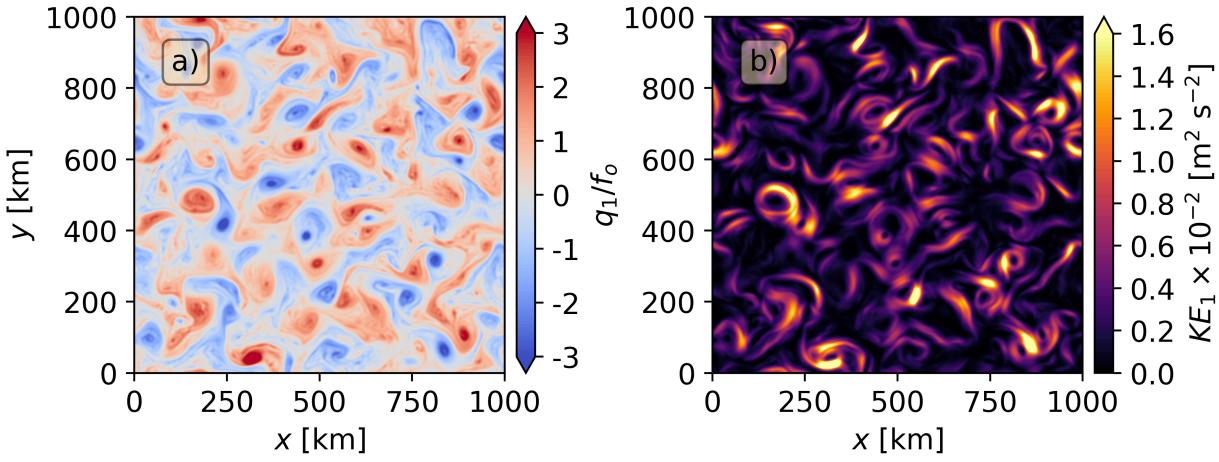

FIG. 1. Upper-layer (a) Coriolis-normalized QG potential vorticity q_1/f_o and (b) KE [m^2 s^{-2}] from the two-layer QG model output for $t = 6$ year.

of $\Delta x = \Delta y \sim 3.9$ km. The simulation is forced with a mean vertical shear, set by $U_1 = 0.025$ m s^{-1} and $U_2 = 0$ in the top and bottom layer of mean thicknesses $H_1 = 500$ m and $H_2 = 2000$ m. The model's deformation radius is prescribed as $R_d = L_d/2\pi = 15$ km rad^{-1}, where $L_d = 92.25$ km is the Rossby deformation wavelength (characteristic of low-latitude environments; Chelton et al. 1998), which is large enough to be well resolved on the chosen grid. Also, $\beta = 1.5 \times 10^{-11}$ m^{-1} s^{-1}, and bottom drag is $r_{ek} = 5.787 \times 10^{-7}$ s^{-1}. The model is spun up for five years and run for an additional 15 years with a time step of 1 hr. For computational convenience, we save and use daily averaged horizontal velocity fields. Since a QG model only simulates the slow dynamics, the impact of this averaging is minimal. We only compute structure functions and spectral quantities for the upper layer.

Velocity differences $\delta\mathbf{u}$ are calculated for all unique grid-point pairs using (1) for each daily step. These velocity differences are then rotated to form longitudinal δu_L and transverse δu_T components via (2), which are then binned into equally spaced r bins spanning between 1 km and 300 km with an average increment of $dr \sim 3.9$ km (i.e., $\sim \Delta x$). Also, since we assume isotropy, we only keep track of pair separation and not the pair orientation. These data from binned pairs form the samples/random variables, whose moments can be calculated to obtain the structure functions at different orders. To estimate the spectral fluxes via (8), and using the RLS fits with (11) and

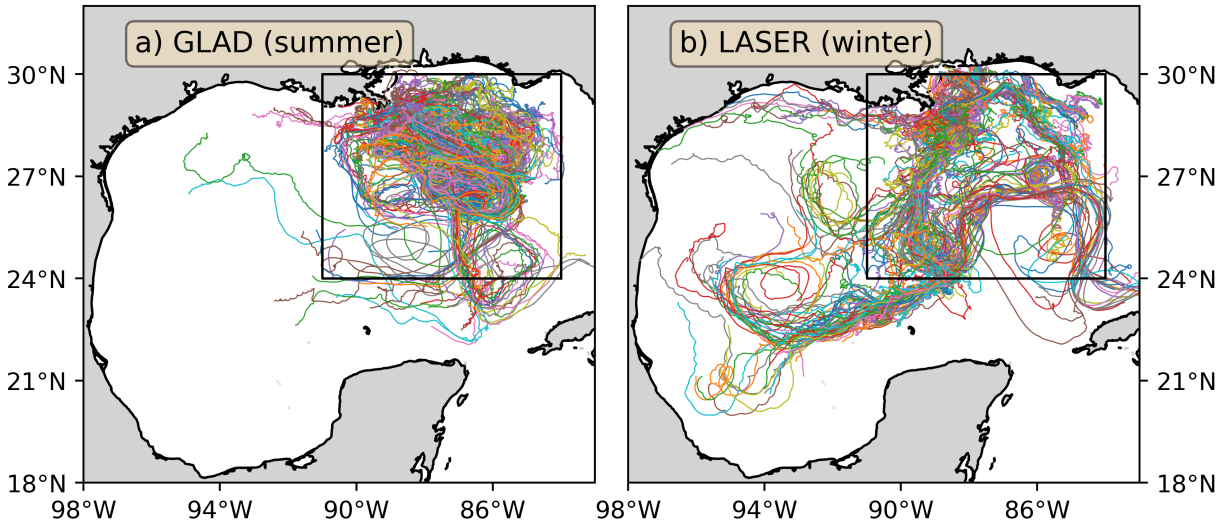

FIG. 2. Drifter trajectories from the (a) GLAD (summer) and (b) LASER (winter) experiments. Each color represents a drifter trajectory. In each panel, the box shows the subset of data used in this analysis and by Balwada et al. (2022).

(14), the wavenumber grid is defined as $k = 0, dk, 2dk, \ldots, k_{N_y}$, where the spacing is $dk = 1/L_x$, and the Nyquist wavenumber is $k_{N_y} = 1/(2\Delta x)$.

2) DRIFTER DATA

We use data from two targeted drifter releases in the northeastern Gulf of Mexico, also used by Balwada et al. (2022). The Grand Lagrangian Deployment (GLAD) experiment released 300 drifters during summer (July-September 2012), and the Lagrangian Submesoscale Experiment (LASER) released approximately 1000 drifters during winter (January-March 2015). These GPS-tracked drifters reported positions at 5-min intervals (position error < 10 m), which were subsequently low-pass filtered with a 1-hour cutoff and sub-sampled to 15 min. Following Balwada et al. (2022), we use a subset of the drifter dataset in waters deeper than 500 m (Fig. 2, box).

To calculate structure functions for this drifter data, we follow Balwada et al. (2022). First, velocity differences are calculated for all possible unique pairs of drifters at every time for each drifter dataset following (1). These velocity differences are then decomposed into δu_L and δu_T via (2) and binned into r bins for all orientations, collecting pairs of overall time sampled by each experiment. Here, the r bins were defined to be logarithmically distributed for 10^1 m $\leq r \leq 10^6$

m as $r_a = r_0 \times 1.5^a$, where $r_0 = 10$ m and $a = (0, 1, 2, 3, \ldots)$ as we expect that flow length scales increase with separation distance. Using linearly spaced bins reduces the number of pairs per bin by two orders of magnitude and produces similar, but noisier, third-order structure function estimates compared to those obtained with log-spaced bins (not shown). These data from binned pairs form the samples/random variables, whose raw moments can be calculated to obtain the structure functions at different orders. We set up the wavenumbers k_j linearly with spacing $dk_j = 1/\max(r)$, and the Nyquist wavenumber is $k_{N_y} = 1/[2(r_2 - r_1)]$. This results in the model matrix $\mathbf{H}$ having more unknowns than data points (i.e., $M > N_r$). Both RLS and NNLS are well-suited for such underdetermined problems.

5. Results

Here, we present the results of applying RLS to the velocity fields from the QG simulation, followed by its application to drifter observations in the Gulf of Mexico. We also thoroughly discuss how uncertainties may be estimated, and we compare RLS-derived results against other approaches when possible. Hereinafter, spectral quantities ($E(k)$, $F(k)$, $F_\Pi(k)$, and ξ_j) are presented as a function of wavenumber k, defined as the inverse wavelength (cycles km^{-1}). All factors of 2π are carried in the calculation of these quantities.

a. Two-Layer Quasi-Geostrophic Turbulence

1) Turbulence phenomenology and KE transfers

The phenomenology of two-layer QG turbulence is more complex than 2D turbulence, but some qualitatively similar features arise (Vallis 2017). The five-year upper-layer isotropic energy spectrum $E(k)$ is calculated by Fourier transforming the daily-averaged horizontal velocity fields (u, v) with no detrending or windowing. The 95% confidence intervals are estimated using the χ^2 distribution and setting the degrees of freedom as the ratio of the length of the time series and its integral time scale (i.e., first zero-crossing in the autocorrelation function). $E(k)$ follows a power law of approximately k^{-4} at higher wavenumbers (blue solid line, Fig. 3a), which indicates forward enstrophy cascade. Between the Rossby deformation wavenumber $k_d = 1/L_d$ and 0.07 cycles km^{-1}, the slope follows a $k^{-5/3}$ law indicative of QG dynamics and changes sign for $k < k_d$. Results based on the last month of hourly-averaged model output (green solid line; Fig. 3a) are

statistically indistinguishable from the five-year average, showing the minimal impact of using daily averaged fields instead of hourly. While the energy spectra are useful diagnostics, by themselves, they provide limited information about the detailed properties of the energy transfers.

In two-layer QG flows, the flow is stirred, or energy is injected into the flow at scales near the Rossby deformation radius R_d by baroclinic instability. Similar to 2D turbulence, we expect an inverse transfer of energy (and a forward transfer of enstrophy) in each layer, and a small forward transfer of energy at high wavenumbers en route to small-scale dissipation. At scales larger than R_d, there is a KE sink near the Rhines scale $R_R = \sqrt{\beta/U}$, which marks the transition scale to a regime where linear Rossby wave dynamics dominate over nonlinear energy transfers (Vallis 2017). At the largest resolved scales, the flow becomes barotropic, and thus some of the energy cascading to larger scales in the top layer is transferred to the lower layer, where it is dissipated by Ekman friction. To confirm this phenomenology, we diagnose the spectral flux $F_\Pi(k)$ from our QG simulation, calculated as the five-year average of the daily spectral flux computed directly in spectral space using (8) and the daily u, v fields. This long-time average ensures a close-to-perfect estimate of the equilibrium spectral flux. Since the domain is doubly periodic, no detrending or windowing was applied (as done for estimating $E(k)$), and horizontal velocity gradients $\nabla_H \mathbf{u}$ are estimated in spectral space. In practice, $F_\Pi(k)$ is computed in two steps: first, the contributions of all Fourier modes within a small wavenumber bin centered at each target wavenumber k_j (i.e., over the interval $k_j - dk/2$–$k_j + dk/2$) are summed; these binned sums represent the kinetic energy injections ξ_j at that scale k_j. Second, the spectral flux $F_\Pi(k)$ is obtained by integrating (cumulative summing) these injections from k_{min} up to the maximum wavenumber k_{N_y}, providing a discrete approximation of the continuous integral in (8).

The KE injections and spectral fluxes for the top layer corroborate the theoretical picture: (i) energy is injected ($\xi_j > 0$) into the flow near the deformation wavenumber $k_d = 1/L_d$ (Fig. 3b), (ii) energy is lost ($\xi_j < 0$) at the Rhines wavenumber $k_R = 1/L_R$ ($L_R = 2\pi r_R$ is the Rhines wavelength; Fig. 3b), and (iii) the energy flux is upscale (inverse) across most scales (Fig. 3c), with a transition to a downscale (forward) transfer at $k > 0.02$ cycles km^{-1} en route to dissipation (small inset, Fig. 3c). Our goal in this section is to estimate the spectral flux expected in QG turbulence (Fig. 3b,c) using the third-order structure function framework (11) (Xie and Bühler 2019; Balwada et al. 2022) and RLS (14) (Wunsch 1996; Kachelein et al. 2022). We further demonstrate that RLS outperforms

NNLS by capturing the full structure of energy injections and transfers, including both positive and negative contributions at each wavenumber.

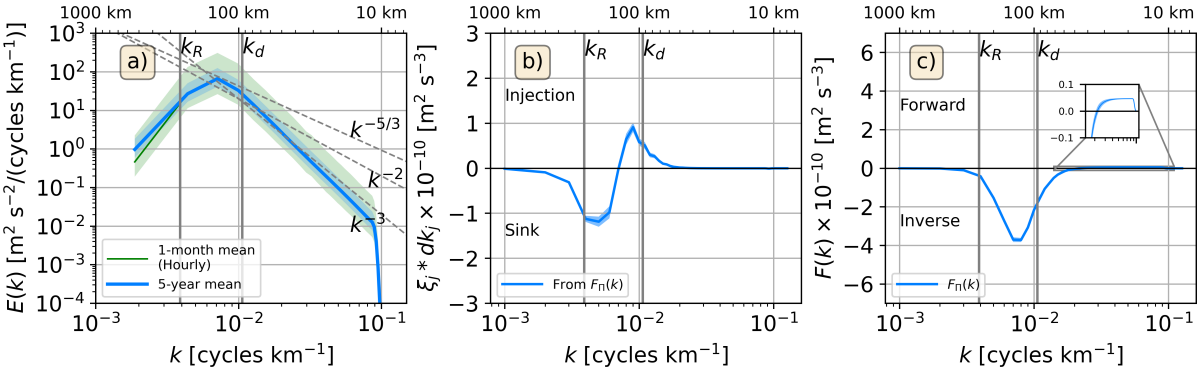

FIG. 3. Five-year mean isotropic KE (a) spectra $E(k)$ [m^2 s^{-2}/ (cycles km^{-1})], (b) injection density per wavenumber spacing $\xi_j * dk_j$ [m^2 s^{-3}], and (c) transfers $F_\Pi(k)$ estimated using (8) [m^2 s^{-3}] (blue solid line). Power laws (gray dashed lines) are shown in (a). Green solid line in (a) is the mean $E(k)$ estimated from one month of hourly averaged model outputs. Shaded areas in (a) show the χ^2 95% confidence intervals. Positive $\xi_j * dk_j$ in (b) indicates KE injection. $k_R = 1/L_R$ and $k_d = 1/L_d$ are the model's Rhines and Rossby deformation wavenumbers (solid gray vertical lines), respectively. Small inset in (c) zooms in on the highest wavenumbers resolved, showing a forward transfer. Positive $F(k)$ in (c) indicates forward KE transfer. The upper log-spaced x-axis is defined as $1/k$ (i.e., wavelength).

2) Samples and uncertainty of third-order structure function

An important assumption for RLS to be optimal is that the prior errors **e** are Gaussian-distributed (Wunsch 1996; Kachelein et al. 2022). In this subsection, we examine the distribution of the pair samples of $D3(r)$ to determine if the errors in $D3(r)$ are Gaussian distributed.

The third-order structure function $D3(r)$ is an ensemble mean of $\delta u3(\mathbf{s},\mathbf{r},t) = \delta u_L(\mathbf{s},\mathbf{r},t)[\delta u_L^2(\mathbf{s},\mathbf{r},t) + \delta u_T^2(\mathbf{s},\mathbf{r},t)]$ over many pair samples coming from different locations, orientations, and times. The distribution of the pair samples $\delta u3(\mathbf{s},\mathbf{r},t)$ is shown as a function of time at two different separations (~ 44 and ~ 83 km) in Fig. 4. For convenience, we only show the first 200 days of the five years; given the setup, the properties of the simulation do not change over time. As expected in turbulent regimes (Barndorff-Nielsen et al. 2004), the δu_3 distributions are non-Gaussian, exhibiting heavy tails and slight skewness, and they vary over time, with intermittent

events reaching between 10 and 35 standard deviations from the mean. These extreme events play a role in setting the mean, and thus $D3(r)$. We conclude that the pair samples of the third-order structure function are non-Gaussian distributed. Consequently, we look for an alternative avenue to generate Gaussian-distributed samples and errors in $D3(r)$.

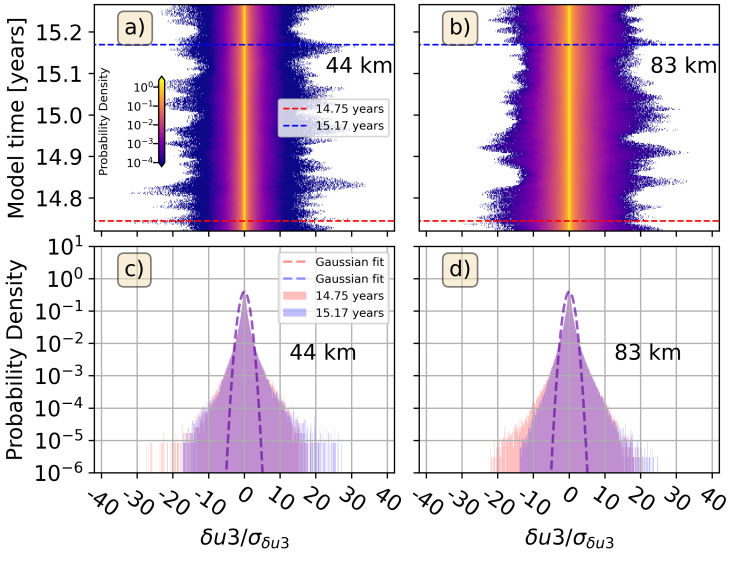

FIG. 4. (a)-(b) Hovmöller diagram of the probability density ($\log_{10}$ scale) of the daily standard-deviation-normalized pair samples of third-order structure function $\delta u3/\sigma_{\delta u3}$ for the (a) 44-km and (b) 83-km r bin. Dashed red and blue lines indicate the 14.75 and 15.17 model years. (c)-(d) Probability density (in $\log_{10}$ scale) of $\delta u3/\sigma_{\delta u3}$ for the (c) 44-km and (d) 83-km r bin. Red and blue bars are the 14.75- and 15.17-year PDFs, respectively. Dashed curves show the Gaussian fit calculated from the mean $\delta u3(\mathbf{s},\mathbf{r},t)$ and standard deviation $\sigma_{\delta u3}$, respectively.

To generate Gaussian-distributed samples, we average the pair samples $\delta u3(\mathbf{s},\mathbf{r},t)$ over the full spatial domain and all orientations of $\mathbf{r}$ ($\overline{\cdots}$), and without any temporal average. Note that this average is meant to be an approximation to the ensemble average ($\langle . \rangle$) of (6). These samples are denoted by $\overline{\delta u3}(r,t)$. Averaging $\delta u3(\mathbf{s},\mathbf{r},t)$ over all orientations and positions results in approximately Gaussian-distributed sample means $\overline{\delta u3}(r,t)$ at each r per the central limit theorem (Stroock 2010). To confirm that $\overline{\delta u3}(r,t)$ is Gaussian distributed, we show PDFs of $\overline{\delta u3}(r,t)$ normalized by the standard deviation of the sample means $\sigma_{\overline{\delta u3}}$ at two separations as examples (Fig. 5a). Visually, these PDFs show that the distribution of sample means is close to Gaussian, confirmed by good agreement with the expected Gaussian distribution (dashed lines), and have

non-zero means. In contrast to the pair samples $\delta u3(\mathbf{s},\mathbf{r},t)$ (Fig. 4), the means and tails of $\overline{\delta u3}(r,t)$ fall within three to four standard deviations (Fig. 5a). Also, the estimated skewness and excess kurtosis at each r indicate that samples are lightly positively skewed, with excess kurtosis < 1 (with moderate tails) (Fig. 5b). Thus, the $\overline{\delta u3}(r,t)$ is approximately Gaussian distributed and satisfies the RLS assumption of Gaussian-distributed errors.

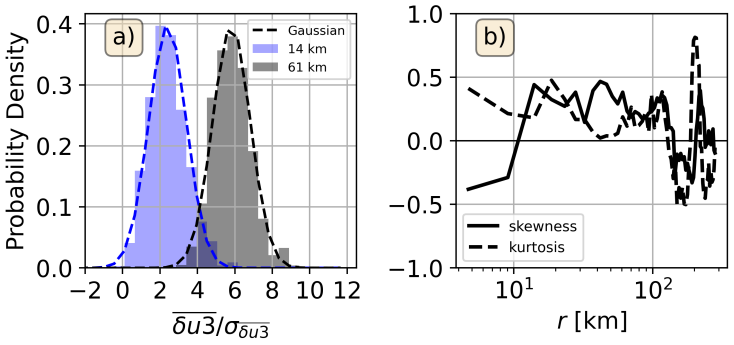

FIG. 5. (a) Probability density of standard-deviation-normalized daily averaged samples $\overline{\delta u3}/\sigma_{\overline{\delta u3}}$ for 14 km (gray) and 61 km (blue) bins calculated using five-year daily averages. Dashed lines show the Gaussian fit. (b) Skewness (solid line) and excess kurtosis (dashed line) as a function of r bin. For a Gaussian distribution, skewness and excess kurtosis are both zero.

3) REGULARIZED LEAST-SQUARES FITTING AND KE TRANSFERS

Here we proceed with the inversion problem using RLS, to test whether a trustworthy estimate of $F(k)$ can be recovered from a given $D3(r)$. The five-year averaged $D3(r)$ is estimated here by time averaging $\overline{\delta u3}(r,t)$. We note that averaged samples $\overline{\delta u3}(r,t)$ (orange solid lines, Fig. 6a) are qualitatively similar to the five-year mean $D3(r)$ (thick black solid line, Fig. 6a). $D3(r)$ for the upper-layer is positive for $r < 100$ km, with a maximum at $r \sim 70$ km, which qualitatively suggests an inverse cascade based on its sign. However, at $r > 100$ km, $D3(r)$ takes on a negative value, even though the spectral transfer $F_\Pi(k)$ exhibits no indication of a forward cascade at these scales (blue solid line, Fig. 6c). This negative lobe in $D3(r)$ is a result of the Bessel function in (7), and stands as a cautionary example of situations when the sign of $D3(r)$ is a misleading indicator of the energy transfer directionality. Thus, it is beneficial to estimate $F(k)$ by inverting (11) rather than relying on the sign of $D3(r)$.

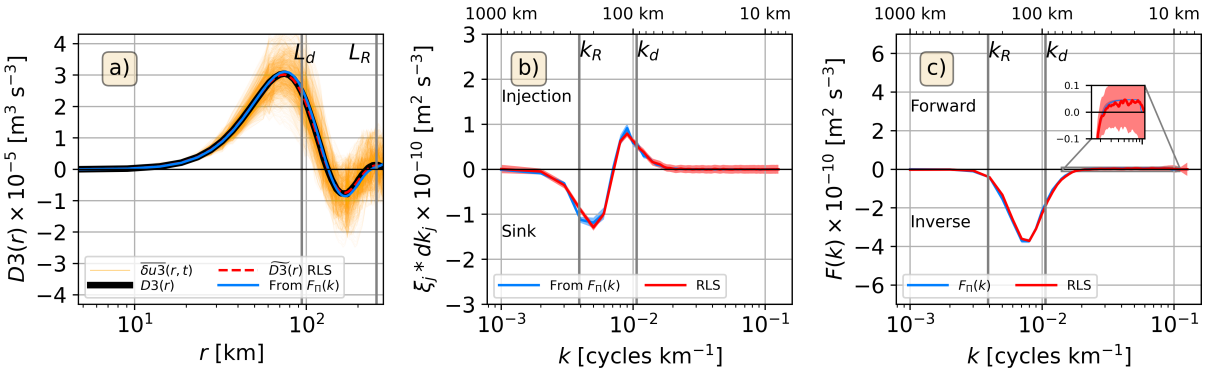

FIG. 6. (a) Third-order structure function $D3(r)$ [m^3 s^{-3}] for the model's upper layer (black thick solid line). Daily $\overline{\delta u3}(r,t)$ (pair samples averaged for all positions and orientations) are shown in orange solid lines. RLS-fitted structure function $\widetilde{D3(r)}$ is shown in thin dashed red line. $D3(r)$ estimated via (7) using the KE transfers calculated using the spectral method $F_\Pi(k)$ from (8) is shown in blue solid line. Solid gray vertical line shows the model's Rossby baroclinic wavelength L_d and Rhine's wavelength L_R. (b) KE injection $\xi_j * dk_j$ (divergence of KE transfers) [m^2 s^{-3}]. Positive values indicate KE injection (divergence). (c) Cross-scale KE transfers $F(k)$ [m^2 s^{-3}]. Positive and negative transfers indicate a forward (downscale) and inverse (upscale) KE transfer. Red and blue solid lines in (b-c) are the RLS-based and spectral estimates (derived from (8)). Shaded red areas in (c-d) are the posterior uncertainty in the injections (15; diag($\sqrt{\mathbf{C_{xx}}}$)) and transfers (16; diag($\sqrt{\mathbf{F_{xx}}}$)). The standard error of the spectral-based estimates is represented by the blue shading. Vertical gray solid lines in (c)-(d) show the model's Rhines wavenumber k_R and Rossby deformation wavenumber k_d. Small inset in (c) zooms in on the highest wavenumbers. The upper log-spaced x-axis in (b)-(c) is defined as $1/k$ (i.e., wavelength).

Apart from the assumptions of Gaussianity inherent to RLS, the structure-function framework described in Section 2 also requires that the flow be homogeneous over the spatial and temporal domain being considered and that the mean flow have no gradients. Since we generated data from a periodic simulation with a prescribed constant background flow, both these assumptions are satisfied by construction (also visually apparent in Fig. 1). However, it should be noted that if we only observed the system over short periods, it would be hard to assess whether the background mean is zero just from the data (see Appendix C). Since the assumptions of the structure-function framework and the RLS approach are satisfied in this context, we proceed to set up the RLS problem. This involves constructing the matrices for the prior data uncertainty $\mathbf{W}$ and the prior uncertainty of the fitted parameters $\mathbf{P}$.

The prior uncertainty of $D3(r)$ is estimated by calculating the standard error, i.e., the standard deviation of the daily averaged samples ($\overline{\delta u 3}(r,t)$; orange solid line, Fig. 5a) divided by the square root of the degrees of freedom $\sqrt{N(r)}$ (see Appendix B for details). Here, the degrees of freedom are not simply the number of days, since $\overline{\delta u 3}(r,t)$ is not an independent sample each day. To estimate $N(r)$, we first calculate the scale-dependent decorrelation time scale $T_{scale}(r)$ following Balwada et al. (2022) via (B1) (black solid line, Fig. B1a). Subsequently, the scale-dependent degrees of freedom $N(r)$ are computed using $T_{scale}(r)$ and the total number of days from (B2) (red solid line, Fig. B1b). We use the square of the standard errors in $D3(r)$ as the diagonal of $\mathbf{W}$; the off-diagonal elements are set to zero.

There is no physical guidance on how to set prior uncertainty for the parameters to be estimated, so we construct $\mathbf{P}$ with the help of a heuristic approach called the "trade-off curve" method (Hansen 2000). The prior uncertainty is chosen to maximize the fit to the data ($D3(r)$) while keeping the size of the fitted parameters ξ_j small. This "sweet spot" is determined by estimating a trade-off between the L2 norm of the estimated ξ_j and the L2 norm of the model-data misfit normalized by the prior uncertainty in $D3(r)$. This heuristic approach is a way to avoid overfitting.

Choosing a larger prior uncertainty for ξ_j slightly reduces the misfit but increases the size of ξ_j (overfits) and the posterior uncertainty. Conversely, the data-model misfit increases as the prior uncertainty decreases (over-smoothed solution). Using this method, the $\mathbf{P}$ diagonal's first element is selected as 10^{-7} m^4 s^{-6} corresponding to the squared prior uncertainty in $\overline{\epsilon}$. Changing the squared uncertainty in $\overline{\epsilon}$ by two orders of magnitude does not alter the shape of the trade-off curve (not shown). For the prior uncertainty in ξ_j (remaining diagonal entries), we set the optimal value to 1×10^{-10} m^6 s^{-6} for all resolved wavenumbers (blue dot, Fig. 7).

With these parameter choices, we perform a fit to $D3(r)$ (thick black solid line, Fig. 6a) to test our RLS approach. KE injections are estimated directly by fitting $D3(r)$ using (11) and (14), as they are the unknowns $\mathbf{x}$. Subsequently, energy transfers $F(k)$ are calculated using (10). The RLS-based energy injections ξ_j (red solid line, Fig. 6b) match both the positive and negative energy injections (blue solid line, Fig. 6b). The RLS $F(k)$ (red solid line, Fig. 6c) indicates the presence of an inverse transfer at almost all k_j and a forward transfer for $k > 0.02$ cycles km^{-1} similar to the spectral transfer $F_\Pi(k)$ (blue solid line, Fig. 6c, inset). The RLS-based structure function $\widetilde{D3}(r)$, obtained by multiplying the model matrix $\mathbf{H}$ with the fitted parameters $\widetilde{\mathbf{x}}$ (red dashed line, Fig. 6a),

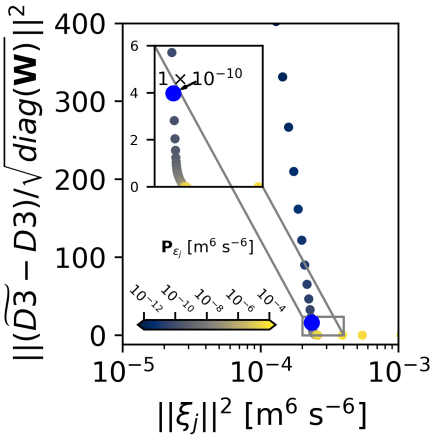

439 FIG. 7. Trade-off L-curve for different squared uncertainties employed for $\mathbf{P}_{\xi_j}$ (color bar). The x-axis shows
440 the L2 norm of the fitted parameters ξ_j [m^6 s^{-6}]. The L2 norm of the residuals normalized by the uncertainty
441 of $D3(r)$ is shown on the y-axis. Small inset shows where the fitted structure function $\widetilde{D3}(r)$ resembles the
442 calculated $D3(r)$. Optimal value $\mathbf{P}_{\xi_j} = 1\times10^{-10}$ m^6 s^{-6} used in this study is shown (blue dot).

451 overlaps with the calculated $D3(r)$ (thick black solid line, Fig. 6a) due to the small residual of the
452 fit. Both curves agree well with the theoretical $D3(r)$ (blue solid line, Fig. 6a), which is derived
453 from $F_\Pi(k)$ (blue solid line, Fig. 6c) via (7).

454 ### 4) Comparing RLS to other estimation approaches

455 We now test whether NNLS fits (used by Balwada et al. 2022) are capable of capturing the
456 properties of the KE injections and transfers expected in the two-layer QG model. To estimate the
457 NNLS-based $\overline{\epsilon}$, ξ_j, and $F(k)$, we first estimated the fitted structure function $\widetilde{D3}(r)$ by averaging
458 $\overline{\delta u3}(r,t)$ and inverted it using NNLS. The fitted structure function $\widetilde{D3}(r)$ is calculated as $\mathbf{H}\widetilde{\mathbf{x}}$. To
459 calculate the standard error, we inverted the daily $\overline{\delta u3}(r,t)$ using NNLS to generate daily estimates
460 of ξ_j, $\overline{\epsilon}$, and $F(k)$. The standard errors in the spectral quantities were then calculated by estimating
461 the standard deviation divided by $\sqrt{N}$, where N is the degrees of freedom at the largest r; this
462 definition of N sets an upper bound for the standard error. As expected, the NNLS method is unable
463 to fit $D3(r)$ for all r (green dashed line, Fig. 8). Consequently, energy injection estimates and
464 spectral transfers are non-physical (green dashed lines, Fig. 8b,c). Therefore, NNLS is ill-suited
465 for estimating convergence of $F(k)$ (i.e., $\xi_j * dk_j < 0$).

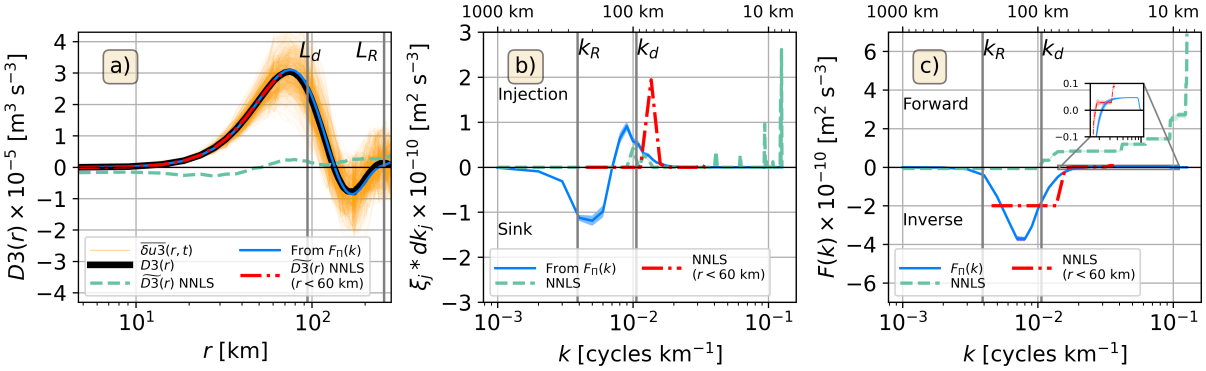

FIG. 8. (a) Third-order structure function $D3(r)$ [m^3 s^{-3}] for the model's upper layer (thick black solid line). Daily $\overline{\delta u 3}(r,t)$ (samples averaged for all positions and orientations) are shown in orange solid lines. $D3(r)$ estimated via (7) using the KE transfers calculated using the spectral method $F_\Pi(k)$ from (8) is shown in blue solid line. Solid gray vertical line shows the model's Rossby baroclinic wavelength L_d and Rhine's wavelength L_R. (b) KE injection $\xi_j * dk_j$ (divergence of KE transfers) [m^2 s^{-3}]. Positive values indicate KE injection (divergence). (c) Cross-scale KE transfers $F(k)$ [m^2 s^{-3}]. Positive and negative transfers indicate a forward (downscale) and inverse (upscale) KE transfer. Green dashed and blue solid lines are the NNLS-based and spectral estimates (derived from (8)). Red dashed-dotted line is the NNLS-based estimates using $D3(r)$ where $r < 60$ km. Colored shading areas show the standard error of the estimated quantities. Small inset in (c) zooms in on the highest wavenumbers. Vertical gray solid lines in (c)-(d) show the model's Rhines wavenumber k_R and Rossby deformation wavenumber k_d. Small inset in (c) zooms in on the highest wavenumbers. The upper log-spaced x-axis in (b)-(c) is defined as $1/k$ (i.e., wavelength).

From (7), we can expect that $F(k)$ for $k > 0.02$ cycles km^{-1} behaves as an increasing function of wavenumber given that $D3(r)$ increases with r for $r < 50$ km (blue solid line, Fig. 8a). This assumption is corroborated by the shape of $F_\Pi(k)$, which is an increasing function for $k > 8\times10^{-3}$ cycles km^{-1} (blue solid line, Fig. 8c). Therefore, we hypothesize that NNLS could potentially capture the size and shape of the ξ_j and $F(k)$ values for $k > 8\times10^{-3}$ cycles km^{-1} (blue solid lines, Fig. 8b,c). A partial fit may help to recover the shape of $F(k)$ over a partial range of scales. The partial fit and estimates and their standard errors are calculated similarly to the full r range.

The NNLS-based structure function $\widetilde{D3}(r)$ over the partial range matches $D3(r)$ well by eye (red dashed-dotted line, Fig. 8a). Unlike the NNLS fit over the full range, the partial $F(k)$ shows the presence of an inverse transfer (red dashed-dotted line, Fig. 8c). However, the estimated energy

injections take on non-zero values at the wrong scale (red dashed-dotted line, Fig. 8b) and are a factor of two larger than the spectral injections (blue solid line, Fig. 8b).

In this section, we have shown that RLS can estimate the KE transfers and injections without assuming a prior shape of $F(k)$ or sign of ξ_j. The RLS method is superior to the NNLS as it constrains the size of the fitted parameters. Also, this approach provides posterior uncertainties for $\overline{\epsilon}$ and ξ_j, and propagates the error to estimate uncertainty in $F(k)$. Having established trust in the RLS approach and the $D3(r)$ framework, we proceed in the next subsection to show the application of the improved methodology to sparse drifter data and compare the ξ_j and $F(k)$ estimated using RLS with those estimated by Balwada et al. (2022) using NNLS.

b. Application to sparse drifter data

1) Pair-sample distribution of $\delta u3$ and uncertainty of $D3(r)$

For the drifter data, as for the QG model, we start by considering for each season the distribution from the pair samples of $\delta u3(\mathbf{s}, \mathbf{r}, t)$, which are averaged over all orientations and positions to estimate the third-order structure function $D3(r)$. In contrast to the dense, gridded sampling from the QG simulations, drifters only sample $\delta u3(\mathbf{s}, \mathbf{r}, t)$ at sparse spatial locations ($\mathbf{s}$) and orientations ($\mathbf{r}$). Also, drifters tend to cluster in convergent flows and/or flows with large vorticity, resulting in biased sampling that can affect both the shape and magnitude of the third-order structure function (Pearson et al. 2020). Corrections for this effect on the first, second, and third-order structure functions have been proposed (Pearson et al. 2019). Nonetheless, Balwada et al. (2022) showed that the direction of KE transfers at $O(1)$ km scales remains unchanged even without such corrections. We proceed with estimating $D3(r)$ and solving the inversion problem for each dataset.

Akin to the QG model (Fig. 4), the distributions from the drifters are highly non-Gaussian, with long tails and occasional outliers as large as $115\sigma_{\delta u3}$ (Fig. 9), as expected for turbulent regimes (Barndorff-Nielsen et al. 2004). Since drifters do not provide a large number of pair samples at a single time, unlike the QG model, we cannot simply average over positions and orientations at a single time, as the limited number of samples would produce noisy estimates. Instead, we seek an alternative method to construct Gaussian-distributed samples of $D3(r)$ to bound the confidence intervals for each dataset.

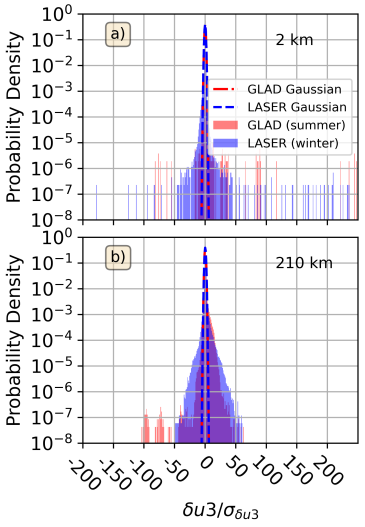

FIG. 9. PDFs of the pairwise samples of third-order structure functions, normalized by their standard deviation ($\delta u_3/\sigma_{\delta u_3}$), for the GLAD (summer; red) and LASER (winter; blue) datasets at (a) ~ 2 km and (b) 210 km bins. The y-axis is shown on a logarithmic scale. Dashed lines indicate the corresponding Gaussian fits.

To estimate these samples and the corresponding uncertainty, we use bootstrapping. Standard bootstrapping assumes that all data samples (pair samples of $\delta u3$ in this case) are independent. Using this approach would yield unrealistically small standard errors (one-to-two orders of magnitude smaller than $D3(r)$), hence small posterior ξ_j, $\overline{\epsilon}$, and $F(k)$ uncertainties (not shown). This happens because many pair samples are correlated due to proximity in space or time, which is not properly accounted for in this standard approach. To overcome this difficulty, we use moving-block bootstrapping, which allows us to estimate uncertainty when the contributing samples are correlated (Kunsch 1989).

For moving-block bootstrapping, we construct a pseudo-time series of $\delta u3(r,t)$ for each r bin from several concatenated time series of different pairs of drifters. The concatenated records inherently have some autocorrelation because of the spatio-temporal proximity between pairs. Then we divide the concatenated $\delta u3(r,t)$ data for each r bin into 50% overlapping blocks of data of size $L(r)/N(r)$, where $L(r)$ is the length of the concatenated data per r bin and $N(r)$ is the number degrees of freedom. Here, $N(r)$ is roughly estimated by dividing the total duration of each drifter experiment by the decorrelation timescale at each r, which was calculated with the help of $D2(r)$ (see Appendix B; Fig. B2). Next, we sample b blocks with replacement at

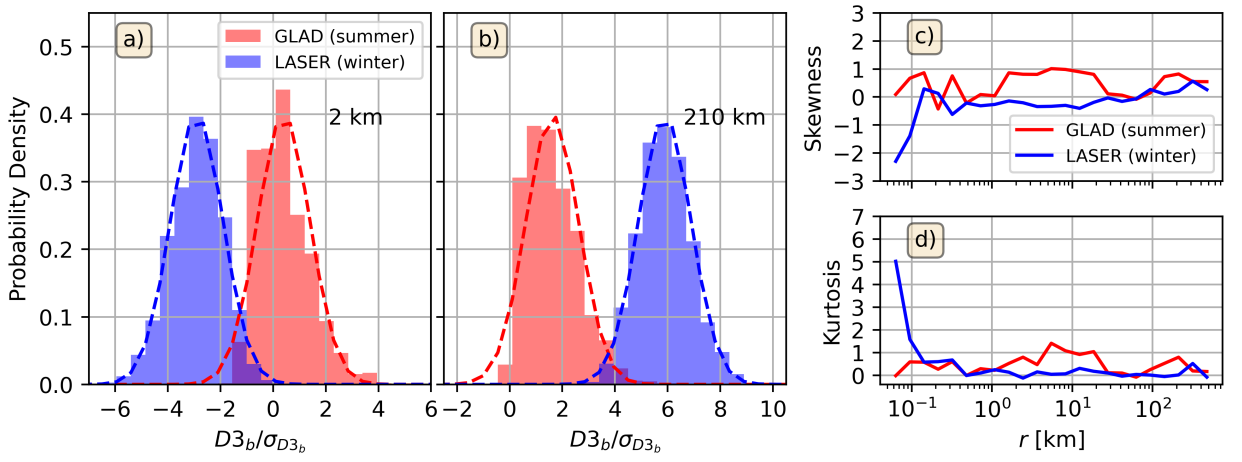

FIG. 10. (a)-(b) PDFs of standard-error-normalized bootstrapped means $D3_b/\sigma_{D3_b}$ generated using moving-block bootstrapping for GLAD (red) and LASER (blue) experiments, respectively. Dashed lines show the Gaussian fits. Only the (a) 2 km and (b) 210 km bins are shown. (c) Skewness and (d) excess kurtosis estimated for the bootstrapped means.

each r and concatenate them to construct a pseudo-time series of $\delta u3(r,t)$ of length $L(r)$. The mean of this pair-sample set gives a bootstrap estimate of $D3(r)$ (denoted as $D3_b(r)$). Bootstrap estimates $D3_b(r)$ are Gaussian-distributed (Stroock 2010) after repeating the procedure 2000 times. This moving-block bootstrapping contrasts with that used by Balwada et al. (2022), where the concatenated block of size $L(r)$ was divided into $N(r)$ blocks.

PDFs of the $D3_b(r)$ for selected r bins show near-Gaussian distributions for both experiments (Fig. 10a,b). PDFs from the GLAD dataset show light positive skewness (red bars, Fig. 10a,b). The near-zero skewness and excess kurtosis for most of the r bins confirm that the bootstrapped quantities have near-Gaussian distributions (Fig. 10c,d). The two smallest r bins for the LASER experiment show large negative skewness and excess kurtosis (blue solid lines, Fig. 10c,d) due to the large outliers in the concatenated data. However, the RLS results are insensitive to the inclusion or removal of these two bins since $J_1(kr)$ in (11) is small for those bins. The prior uncertainty in $D3(r)$ was estimated by computing the standard deviation of these bootstrapped $D3_b(r)$ distributions.

2) KE transfers from sparse drifter data

Next, we apply the RLS approach to deduce the seasonality of the KE transfers and injection rates by inverting (11) with the estimated $D3(r)$ from the summertime GLAD and wintertime LASER experiments (Fig. 11a,b). $D3(r)$ for each dataset was calculated by replacing the ensemble averaging (6) with an average of all pair samples $\delta u3$ per r bin, which is the same as the mean estimated from the samples generated by the modified bootstrapping approach. The summertime $D3(r)$ could indicate that $F(k)$ does not purely increase with k since $D3(r)$ decreases slightly between 10 km $\leq r \leq$ 60 km (dark red solid; Fig. 11a), which could indicate convergence of $F(k)$ (i.e., $\xi_j < 0$). The wintertime $D3(r)$ qualitatively suggests the presence of bidirectional energy transfers as they transition from negative to positive values as r increases (dark blue solid line, Fig. 11b); the slight decrease in $D3(r)$ for $r < 1$ km suggests a weakening of the forward transfer. We note that the first-order structure function $D1(r)$ for both seasons shows that the condition of homogeneity is not satisfied for all r with the limited sampling (i.e., $D1(r) \neq 0$; see Appendix C, Fig. C2). We proceed with caution in interpreting our results.

To set up the RLS method, the diagonal entries of $\mathbf{W}$ are set as the squared uncertainty in $D3(r)$ (shaded areas, Fig. 11a,b). We set the squared uncertainty in $\overline{\epsilon}$ to 1×10^{-7} m^4 s^{-6} (first entry of the diagonal of $\mathbf{P}$), whereas the squared prior uncertainty of ξ_j (the remaining diagonal entries) as 4×10^{-4} m^6 s^{-6} after using the "L-curve" method (not shown). To test sensitivity, we varied the squared uncertainty in $\overline{\epsilon}$ by three orders of magnitude and found that the RLS results were unaffected. We also compared our RLS estimates with estimates derived using NNLS (Balwada et al. 2022). To estimate the uncertainty in the NNLS-based ξ_j and $F(k)$ for each season per r bin, we invert the 2000 bootstrap means $D3_b(r)$ to estimate 2000 bootstrapped ξ_j (11) and $F(k)$ (10).

The RLS-based $D3(r)$ (black solid lines, Fig. 11a,b) matches the observed $D3(r)$ (dark red and blue solid lines, Fig. 11a,b) better than the NNLS fit (light red and blue solid lines, Fig. 11a,b) for both seasons. The NNLS fit (light red solid line) fails to capture the slight decrease in magnitude in the GLAD $D3(r)$ located at $r \sim 60$ km (dark red solid line). The RLS-based estimates of ξ_j (black solid lines, Fig. 11c,d) are smoother and smaller in amplitude (though also statistically not different from zero) than the NNLS estimates (light red and blue solid lines, Fig. 11c,d and insets). Moreover, the NNLS fit fails to estimate any negative energy injection rates by design, whereas

the RLS-based ξ_j values suggest the presence of such negative injections, as seen in the summer at intermediate scales of $k \sim 0.07$ cycles km^{-1} (black solid line, small inset in Fig. 11c).

The spectral flux $F(k)$ estimated using RLS (black solid lines, Fig. 11e,f) follows a shape and amplitude similar to those estimated using NNLS (light red and blue solid lines, Fig. 11e,f, respectively): a bidirectional KE transfer, where an inverse transfer dominates at mesoscales, and forward transfer is present at submesoscales. The transition scale from inverse to forward transfer shows a seasonal modulation. Both the spectral fluxes (10), whether estimated using RLS or NNLS (Fig. 11e,f), take on a negative value (inverse transfer) at the smallest wavenumber k_1 as $\overline{\epsilon}$ estimated from (11) is positive (not shown). The RLS- and NNLS-based $F(k)$ estimates are not statistically distinguishable for each season. Unlike the NNLS fits, which show $F(k)$ to be statistically different from zero at nearly every k_j in both seasons, the RLS fits reveal that the summer forward transfer at submesoscales ($k > 1$ cycles km^{-1}) is not statistically distinguishable from zero (black solid line and gray shading, Fig. 11e). These results suggest that the summertime forward transfer at submesoscales is more variable than in winter, likely reflecting the prevalence of many weaker events alongside a few strong ones (black solid line and gray shading, Fig. 11f).

6. Summary and Discussion

We have presented an improved methodology to estimate cross-scale KE transfers $F(k)$ and injection rates ξ_j from third-order structure functions $D3(r)$, extending the framework of Xie and Bühler (2019) and Balwada et al. (2022). The RLS method constrains the size of the fitted parameters by incorporating prior uncertainty and reduces overfitting, yielding physically realistic KE injection rates. In contrast, ordinary and non-negative least squares may produce unconstrained non-physical rates. Tests with a two-layer QG model that generates an eddy-rich mesoscale field show that RLS accurately captures the inverse energy transfer ($F(k) < 0$) and the convergence of KE transfers ($\xi_j < 0$) expected in QG turbulence (Figs. 6). In contrast, NNLS fails to detect convergences because it enforces only positive injection rates (Fig. 8).

Applied to the GLAD (summer) and LASER (winter) drifter datasets, both RLS and NNLS recover the expected bidirectional KE transfer, with $F(k)$ transitioning from inverse to forward as k increases and the transition scale shifting seasonally from $k \sim 1$ cycles km^{-1} in summer to $k \sim 0.02$ cycles km^{-1} in winter (Fig. 11). However, only RLS identifies KE convergence ($\xi_j < 0$) at

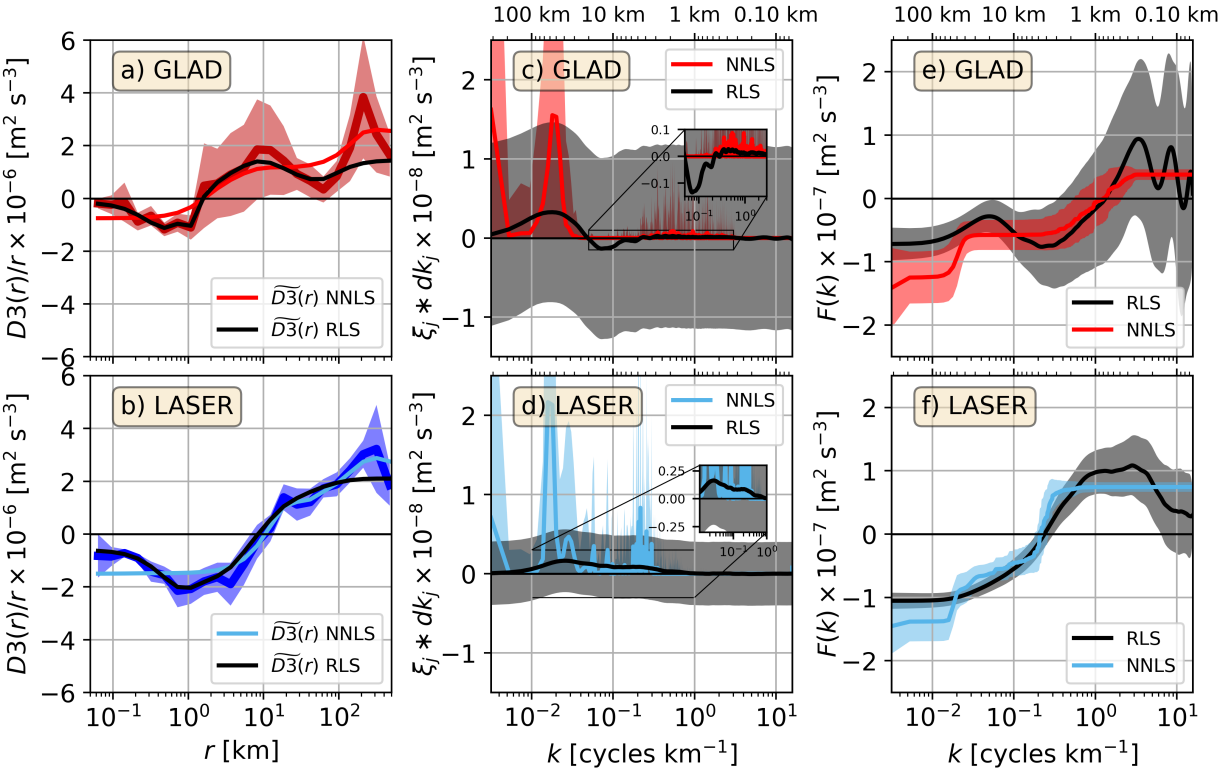

597 FIG. 11. (a)-(b) Normalized third-order structure function $D3(r)/r$, (c)-(d) KE injections rates $\xi_j dk_j$ [m^2 s^{-3}]
598 and (e)-(f) KE transfers $F(k)$ [m^2 s^{-3}]. Dark red (a) and blue (b) solid lines show the structure function from
599 GLAD (summer) and LASER (winter) datasets, respectively. Black solid line represents the variables estimated
600 using RLS. Shaded areas in (a)-(b) are the prior uncertainties of $D3(r)$. Light red and blue solid lines show the
601 NNLS-based results. Colored and gray-shaded areas are the NNLS-based bootstrapped standard error and the
602 RLS posterior uncertainties, respectively. Positive and negative ξ_j in (c)-(d) indicate KE injection (divergence
603 of KE transfer) and sink (convergence), respectively. Forward (downscale) and inverse (upscale) transfer are
604 denoted by positive and negative $F(k)$ in (e)-(f). k_j are linearly spaced with $dk_j = 1/\max(r)$. Small insets in
605 (c) and (d) zoom in on the RLS-based injections. The upper log-spaced x-axis in (c)-(f) is defined as $1/k$ (i.e.,
606 wavelength).

621 intermediate scales ($k \sim 0.07$ cycles km^{-1} in summer; $k \sim 9 \times 10^{-3}$ cycles km^{-1} in winter), which
622 enhances the inverse transfer and shifts the transition to forward transfer toward smaller scales.
623 These convergences, undetected by NNLS, may arise from wind-driven damping (Renault et al.
624 2018), vertical KE transfer below the mixed layer, or conversion to potential energy, motivating
625 future work combining this methodology with stratified turbulence diagnostics.

In contrast to the QG model where RLS-based ξ_j's are statistically different from zero (Fig. 6b), both the RLS-based injection ξ_j's are statistically indistinguishable from zero (Fig. 11c,d), with larger uncertainties found for the summertime experiment than for the wintertime. These large uncertainties in the ξ_j's likely arise from the limited sampling of drifters, from biases caused by their tendency to accumulate in convergent coherent flow structures (Pearson et al. 2019, 2020), and from the short residence time in regions of large KE. Nonetheless, these limitations, which are inherent to the drifter sampling, do not prevent inferring the cross-scale KE transfers. The third-order structure function framework and the RLS fits yield robust and statistically different-from-zero estimates of both the magnitude and direction of the transfers (Fig. 11e,f). Therefore, despite their sampling limitations, drifters remain sufficiently informative for diagnosing properties of the KE transfers.

Adequately estimating the prior uncertainty in $D3(r)$ is crucial for accurately estimating the KE injections and transfers, as it has a significant impact on the posterior uncertainty in ξ_j and $F(k)$. An alternative approach for estimating prior uncertainties in $D3(r)$ inherent in limited sampling settings is parametric bootstrapping, where the data are adjusted to a PDF such as a normal-inverse Gaussian distribution (DeMarco and Basu 2017; Barndorff-Nielsen et al. 2004) that best fits the data PDF (potentially using maximum likelihood estimation), and then bootstrapping is carried out using the adjusted data. This method has proved useful, yielding uncertainties in high-order structure functions with relatively less bias (DeMarco and Basu 2017). Additionally, the posterior uncertainty in ξ_j, $\overline{\epsilon}$, and $F(k)$ could be improved by including a full error budget for the prior uncertainty in $D3(r)$ accounting for sampling biases, instrument errors, and cross-correlations across observations (e.g., drifters; Spydell et al. 2019). Likewise, the posterior uncertainty in ξ_j could be improved in future work by modeling the diagonal entries of $\mathbf{P}$ as red noise proportional to k^{-2} (Kachelein et al. 2022), such that the prior uncertainty in ξ_j decreases towards small wavenumbers.

This study demonstrates that the improved methodology, when combined with the $D3(r)$ framework, can be applied to both gridded and sparse, ungridded datasets. In contrast, spectral and coarse-graining methods require gridded data to estimate velocity gradients (Srinivasan et al. 2023; Ajayi et al. 2021). Advective structure functions (Pearson et al. 2021) are particularly useful for estimating KE and enstrophy transfers in anisotropic flows, yet still require gridded data to

calculate velocity gradients. Most ocean observations, such as drifters, shipboard acoustic Doppler current profiler transects, and autonomous platforms, provide ungridded velocity data, which can now be leveraged to quantify and analyze the KE transfer using the methodology presented here. A deeper understanding of the KE transfer has the potential to refine existing ocean parameterizations and inspire new ones for global climate models.

Data availability statement. The code for the PyQG model is made available in `https://doi.org/10.5281/zenodo.6380711`, and documentation is available in `https://pyqg.readthedocs.io/en/latest/`. The GLAD and LASER experiment drifter data can be accessed in `https://data.gulfresearchinitiative.org/`. Python code for processing the GLAD and LASER drifter datasets, running the QG simulation, and estimating structure functions and spectral fluxes using regularized least-squares is available at `https://github.com/manuelogtzv/SF3_RLS`. Arch 6.3.1 (Python library) used to estimate the moving-block bootstrapping (Sheppard et al. 2024) is available in `https://arch.readthedocs.io/en/latest/index.html` and `https://zenodo.org/records/10981635`.

Acknowledgments. M. O. G. V., S. T. G., and M. M. have been supported by the NASA Surface Water and Ocean Topography Science Team (NASA 80NSSC20K1136, 80NSSC24K1657), the NASA Ocean Vector Winds Science Team (80NSSC19K0059, 80NSSC23K0979), and the NASA Ocean Surface Topography Science Team (80NSSC21K1822). D. B. acknowledges support from NSF grant OCE-2242110. B. C. acknowledges support from ONR grant N000142112726. M. M. acknowledges NASA grants 80GSFC20C0101 and NOAA grants NA23NOS4000334, NA20OAR4320278, and NA23OAR0110318. M. O. G. V. and D. B. acknowledge funding from NSF through the Learning the Earth with Artificial Intelligence and Physics (LEAP) Science and Technology Center (STC) (Award #2019625).

APPENDIX A

Equations for two-layer QG model

In this appendix, we provide details about the equations solved in the two-layer QG model (PyQG; Abernathey et al. 2022). The model uses QG potential vorticity in the upper q_1 and lower q_2 layers as prognostic variables:

$$q_m = \nabla_H^2 \Psi_m + (-1)^m F_m (\Psi_1 - \Psi_2), \quad m = 1, 2 \tag{A1}$$

where Ψ_m is geostrophic streamfunction in layer m with thickness H_m, $F_1 = k_d^2/(1+\alpha)$, and $F_2 = \alpha F_1$, where

$$k_d^2 = \frac{f_o^2}{g'} \frac{H_1 + H_2}{H_1 H_2} \tag{A2}$$

is the baroclinic Rossby deformation wavenumber, $\alpha = H_1/H_2$ is the layer thickness ratio, f_o is the local Coriolis frequency, and g' is reduced gravity. Ψ_m is diagnosed from q_m by integrating the Laplacian using periodic boundary conditions. The horizontal velocity components are calculated using the Ψ_m:

$$u_m = -\partial_y \Psi_m, \quad v_m = \partial_x \Psi_m. \tag{A3}$$

The model solves the evolution of the QG potential vorticity field in spectral space $\Psi_m = \sum \widehat{\Psi}_m e^{i(k_x \cdot x + k_y \cdot y)}$:

$$\partial_t \widehat{q}_m = -\widehat{\mathrm{J}}(\Psi_m, q_m) - \mathrm{i} k_x \beta \widehat{\Psi}_m - \mathrm{i} k_x U_m \widehat{\Psi}_m + \delta_{m,2} r_{ek} k^2 \hat{\Psi}_2 + \widehat{\mathrm{SSD}}, \tag{A4}$$

where U_m is the background flow, ∂_t is the Eulerian time derivative, and $\mathrm{J}(\Psi_m, q_m) = \partial_x \Psi_m \partial_y q_m - \partial_y \Psi_m \partial_x q_m$ is the Jacobian in physical space. The change in the Coriolis frequency with latitude y is defined as $f_o + \beta y$ with a slope β. $\delta_{m,2}$ is the Kronecker delta function, and r_{ek} is the bottom drag coefficient applied only to the second layer to dissipate large-scale energy. The small-scale dissipation, SSD, absorbs enstrophy that cascades toward small scales and is set as an exponential filter:

$$E_f(k^*) = \begin{cases} 1 & k^* < k_c \\ e^{-23.6(k^* - k_c)^4}, & k^* \geq k_c \end{cases}, \tag{A5}$$

where $k^* = \sqrt{(k_x\Delta x)^2 + (k_y\Delta y)^2}$ is the non-dimensional wavenumber, $\Delta x = \Delta y = 3.9$ km are the spatial grid spacing, and $k_c = 0.65\pi$ is the non-dimensional cut-off wavenumber. The filter reduces aliasing errors and provides stable simulations with necessary numerical dissipation (Ross et al. 2023), and attenuates the highest third of wavenumbers of all terms in the right side of (A4). More details about the model's solution are found in Abernathey et al. (2022).

APPENDIX B

Second-order structure function and degrees of freedom

Here we show the second-order structure function $D2(r)$ and the degrees of freedom estimated from the QG model u, v outputs, and the drifter data. We follow Balwada et al. (2022) and employ $D2(r)$ to estimate the degrees of freedom $N(r)$ as

$$T_{scale}(r) = r/\sqrt{D2(r)}, \tag{B1}$$

$$N(r) = T_{tot}/T_{scale}(r), \tag{B2}$$

where T_{tot} is the duration of the model's time series used for the analysis (5 years) and 90 and 60 days for the summer GLAD and wintertime LASER drifter data sets, respectively.

QG model

We transform $E(k)$ (blue solid line, Fig. 3a) to second-order structure function $D2(r)$ via (4) and compare it to $D2(r)$ calculated directly from the model's velocity output (Fig. B1a). The theoretical $D2$ (blue solid line) lies on top of the estimated $D2$ (black solid line) and within the spatially-averaged estimates $\overline{\delta u2}(r,t)$ (red solid line) (Fig. B1a) following a r^2 power law for $r \leq 20$ km. The theoretical and estimated $D2(r)$ show a shallower r relationship for 30 km$< r < 70$ km. We used $D2(r)$ to estimate $T_{scale}(r)$ with (B1) and $N(r)$ via (B2); the latter is employed to estimate the uncertainty in $D3(r)$. As expected, larger flows decorrelate more slowly than small-scale flows (black solid line); consequently, $N(r)$ decreases with r (red solid line) (Fig. B1b).

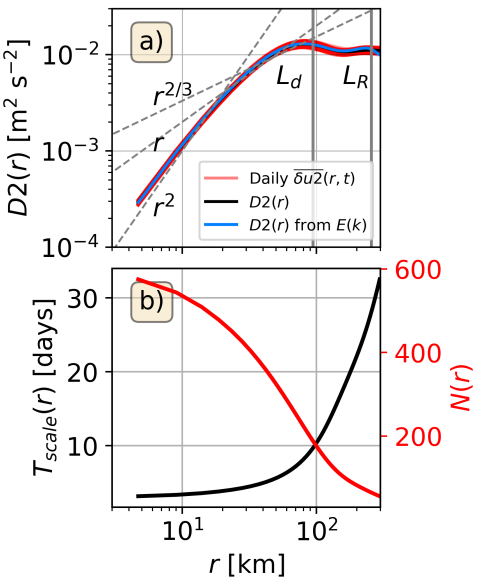

FIG. B1. (a) Second-order structure function $D2(r)$ [m^2 s^{-2}]. Red solid lines represent daily estimates $\overline{\delta u2}(r,t)$. Black and blue solid lines are the five-year mean $D2(r)$ and the structure function estimated from $E(k)$, respectively. Power laws are shown in dashed gray lines. The Rossby deformation wavelength L_d and the Rhines wavelength L_R are indicated by vertical gray solid lines. (b) Decorrelation time scale $T_{scale}(r)$ [days] (black solid line; left y-axis) and degrees of freedom $N(r)$ (red solid line; right y-axis) estimated using (B1) and (B2), respectively and setting $T_{tot} = 5$ years.

Drifter data

Following Balwada et al. (2022), we estimated $D2(r)$ by replacing the ensemble averaging of $\delta u2(\mathbf{s},\mathbf{r},t)$ by averaging all samples per r bin. Submesoscales with scales $r < 10$ km are more energetic during the winter (blue solid line) than in summer (red solid line), whereas mesoscales ($r > 10$ km) are more energetic during the summer than winter (Fig. B2a). The energizing of submesoscales in winter is likely driven by energetic submesoscale mixed layer instabilities that convert potential energy stored in the winter deep mixed layer to KE at the scales of the mixed layer deformation radius (Callies et al. 2015; Balwada et al. 2022). As in the model, $T_{\text{scale}}(r)$ estimated using (B1) increases linearly with r in log-log space (red and blue solid lines, Fig. B2b). At submesoscales, summertime T_{scale} (red solid line) exhibits slightly shorter $T_{\text{scale}}(r)$ than wintertime (blue solid line). $N(r)$ decreases with r with summertime (red dotted line) having slightly more

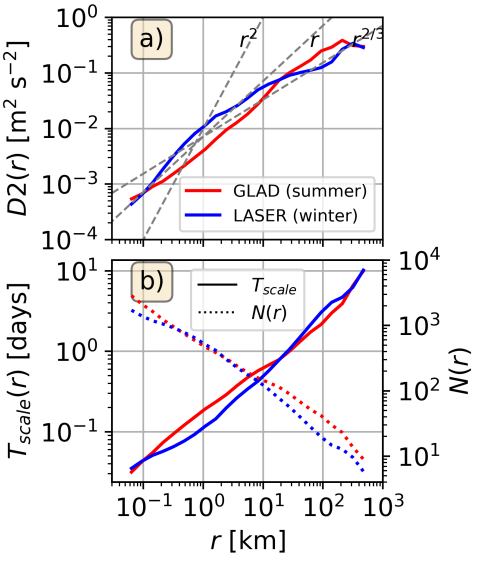

FIG. B2. (a) Second-order structure function $D2(r)$ [m^2 s^{-2}] for the GLAD (red solid line) and LASER (blue solid line) experiments. Power laws are shown in dashed gray lines. (b) Decorrelation time scale $T_{scale}(r)$ [days] (solid lines) and degrees of freedom $N(r)$ (dotted lines) estimated by setting $T_{tot} = 90$ days and 60 days for the GLAD and LASER experiments, respectively.

$N(r)$ than in winter (blue dotted line) (except for 10^{-1} km $< r < 10^{1}$ km) as the summertime experiment's duration is larger than that in winter (Fig. B2b).

APPENDIX C

First-order structure function

An important requirement for the structure-function theory is that the flow must be homogeneous, i.e., $D1(r) = 0$ for any length scale r (Frisch 1995). The mean current can determine the sign and magnitude of the $D3(r)$, limiting the application of the $D3(r)$ framework. In this appendix, we calculated $D1(r)$ from the velocity fields in the model and drifter data using (3) to analyze whether the homogeneity condition is fulfilled.

Two-layer QG model

Daily $\overline{\delta u 1}(r,t)$ is shown in Fig. C1a along with the five-year ensemble averaged $D1(r)$. The daily snapshots (orange solid line) variability increases with separation r. The mean $D1(r)$ (black solid

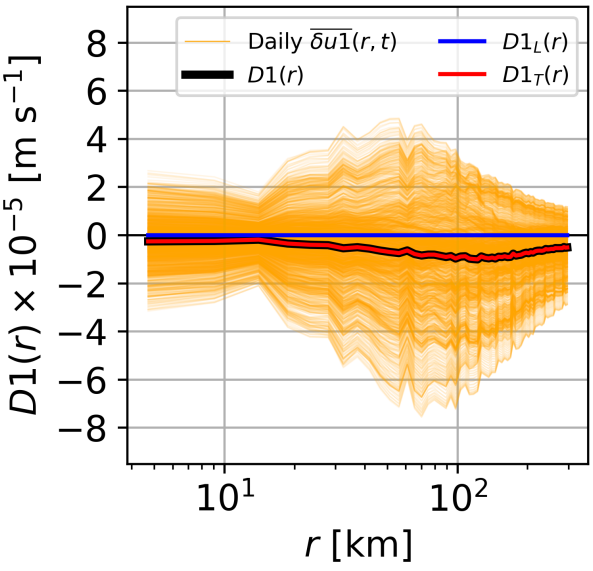

FIG. C1. Upper-layer five-year first-order structure function $D1(r)$ [m s^{-1}]. Orange lines are daily $\overline{\delta u1}(r,t)$. Black, blue, and red solid lines are the five-year ensemble-averaged $D1$, longitudinal $D1_L(r)$, and transverse $D1_T(r)$ structure functions.

line) is almost zero for $r < 20$ km but becomes statistically different from zero at the larger scales. Since the longitudinal component is linked to divergent flows (Pearson et al. 2020), the five-year mean longitudinal structure function $D1_L(r)$ (blue solid line) vanishes because the model flow field is purely rotational, as expected in QG flows. Consequently, only the transverse component $D1_T(r)$ (red solid line) contributes to the total structure function $D1(r)$.

Drifter data

First-order structure function $D1(r)$ (Fig. C2) for the GLAD (summer; red solid line) and LASER (winter; blue solid line) datasets show that the background flow has a large contribution across different flow scales, with a larger contribution at the mesoscales ($r \sim O(10^2)$ km) and during wintertime. Surface drifters converging into individual flow features such as mesoscale eddies and large-scale currents (Fig. 1) could result in highly heterogeneous sampling (Pearson et al. 2020).

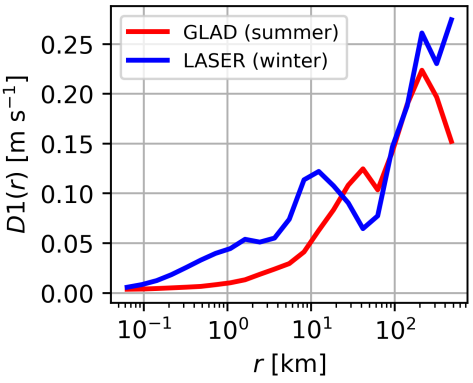

FIG. C2. First-order structure function $D1(r)$ [m s^{-1}] for the GLAD (summer; red solid line) and LASER (winter; blue solid line) experiments.

References

Abernathey, R., and Coauthors, 2022: PyQG. Zenodo, doi:https://doi.org/10.5281/zenodo.6563667.

Ajayi, A., J. Le Sommer, E. P. Chassignet, J.-M. Molines, X. Xu, A. Albert, and W. Dewar, 2021: Diagnosing Cross-Scale Kinetic Energy Exchanges From Two Submesoscale Permitting Ocean Models. *Journal of Advances in Modeling Earth Systems*, **13 (6)**, e2019MS001 923, doi:https://doi.org/10.1029/2019MS001923.

Aluie, H., M. Hecht, and G. K. Vallis, 2018: Mapping the Energy Cascade in the North Atlantic Ocean: The Coarse-Graining Approach. *Journal of Physical Oceanography*, **48 (2)**, 225 – 244, doi:10.1175/JPO-D-17-0100.1.

Balwada, D., J. H. LaCasce, and K. G. Speer, 2016: Scale-dependent distribution of kinetic energy from surface drifters in the Gulf of Mexico. *Geophysical Research Letters*, **43 (20)**, 10,856–10,863, doi:https://doi.org/10.1002/2016GL069405, URL https://agupubs.onlinelibrary.wiley.com/doi/abs/10.1002/2016GL069405, https://agupubs.onlinelibrary.wiley.com/doi/pdf/10.1002/2016GL069405.

Balwada, D., Q. Xiao, S. Smith, R. Abernathey, and A. R. Gray, 2021: Vertical fluxes conditioned on vorticity and strain reveal submesoscale ventilation. *Journal of Physical Oceanography*,

51 (9), 2883 – 2901, doi:10.1175/JPO-D-21-0016.1, URL https://journals.ametsoc.org/view/journals/phoc/51/9/JPO-D-21-0016.1.xml.

Balwada, D., J.-H. Xie, R. Marino, and F. Feraco, 2022: Direct observational evidence of an oceanic dual kinetic energy cascade and its seasonality. *Science Advances*, **8 (41)**, eabq2566, doi:10.1126/sciadv.abq2566.

Barndorff-Nielsen, O. E., P. Blæsild, and J. Schmiegel, 2004: A parsimonious and universal description of turbulent velocity increments. *The European Physical Journal B-Condensed Matter and Complex Systems*, **41 (3)**, 345–363, doi:https://doi.org/10.1140/epjb/e2004-00328-1.

Bennett, A. F., 1984: Relative dispersion: Local and nonlocal dynamics. *Journal of Atmospheric Sciences*, **41 (11)**, 1881 – 1886, doi:10.1175/1520-0469(1984)041<1881:RDLAND>2.0.CO;2.

Callies, J., R. Ferrari, J. M. Klymak, and J. Gula, 2015: Seasonality in submesoscale turbulence. *Nature Communications*, **6 (1)**, 6862, doi:https://doi.org/10.1038/ncomms7862.

Capet, X., J. C. McWilliams, M. J. Molemaker, and A. F. Shchepetkin, 2008: Mesoscale to Submesoscale Transition in the California Current System. Part III: Energy Balance and Flux. *Journal of Physical Oceanography*, **38 (10)**, 2256 – 2269, doi:10.1175/2008JPO3810.1, URL https://journals.ametsoc.org/view/journals/phoc/38/10/2008jpo3810.1.xml.

Chelton, D. B., R. A. deSzoeke, M. G. Schlax, K. E. Naggar, and N. Siwertz, 1998: Geographical Variability of the First Baroclinic Rossby Radius of Deformation. *Journal of Physical Oceanography*, **28 (3)**, 433 – 460, doi:10.1175/1520-0485(1998)028<0433:GVOTFB>2.0.CO;2, URL https://journals.ametsoc.org/view/journals/phoc/28/3/1520-0485_1998_028_0433_gvotfb_2.0.co_2.xml.

Cho, J. Y. N., and E. Lindborg, 2001: Horizontal velocity structure functions in the upper troposphere and lower stratosphere: 1. Observations. *Journal of Geophysical Research: Atmospheres*, **106 (D10)**, 10 223–10 232, doi:10.1029/2000JD900814.

DeMarco, A. W., and S. Basu, 2017: Estimating higher-order structure functions from geophysical turbulence time series: Confronting the curse of the limited sample size. *Physical Review E*, **95 (5)**, 052 114, doi:https://doi.org/10.1103/PhysRevE.95.052114.

Dong, J., B. Fox-Kemper, H. Zhang, and C. Dong, 2020: The Seasonality of Submesoscale Energy Production, Content, and Cascade. *Geophysical Research Letters*, **47 (6)**, e2020GL087 388, doi:https://doi.org/10.1029/2020GL087388.

Ferrari, R., and C. Wunsch, 2009: Ocean circulation kinetic energy: Reservoirs, sources, and sinks. *Annual Review of Fluid Mechanics*, **41 (1)**, 253–282, doi:https://doi.org/10.1146/annurev.fluid.40.111406.102139.

Freilich, M., L. Lenain, and S. T. Gille, 2023: Characterizing the Role of Non-Linear Interactions in the Transition to Submesoscale Dynamics at a Dense Filament. *Geophysical Research Letters*, **50 (15)**, e2023GL103 745, doi:https://doi.org/10.1029/2023GL103745.

Frisch, U., 1995: *Turbulence: the legacy of A. N. Kolmogorov*. Cambridge university press.

Hansen, P., 2000: The L-curve and its use in the numerical treatment of inverse problems. *InviteComputational Inverse Problems in Electrocardiology*, WIT Press, inviteComputational Inverse Problems in Electrocardiology ; Conference date: 01-01-2000.

Kachelein, L., B. D. Cornuelle, S. T. Gille, and M. R. Mazloff, 2022: Harmonic Analysis of Non-Phase-Locked Tides with Red Noise Using the red tide Package. *Journal of Atmospheric and Oceanic Technology*, **39 (7)**, 1031 – 1051, doi:https://doi.org/10.1175/JTECH-D-21-0034.1.

Kolmogorov, A. N., 1991: The local structure of turbulence in incompressible viscous fluid for very large Reynolds numbers. *Proceedings of the Royal Society of London. Series A: Mathematical and Physical Sciences*, **434 (1890)**, 9–13.

Kunsch, H. R., 1989: The Jackknife and the Bootstrap for General Stationary Observations. *The Annals of Statistics*, **17 (3)**, 1217 – 1241, doi:10.1214/aos/1176347265, URL https://doi.org/10.1214/aos/1176347265.

Lindborg, E., 1999: Can the atmospheric kinetic energy spectrum be explained by two-dimensional turbulence? *Journal of Fluid Mechanics*, **388**, 259–288, doi:10.1017/S0022112099004851.

Lindborg, E., and J. Y. N. Cho, 2001: Horizontal velocity structure functions in the upper troposphere and lower stratosphere: 2. Theoretical considerations. *Journal of Geophysical Research: Atmospheres*, **106 (D10)**, 10 233–10 241, doi:https://doi.org/10.1029/2000JD900815.

Naveira Garabato, A. C., X. Yu, J. Callies, R. Barkan, K. L. Polzin, E. E. Frajka-Williams, C. E. Buckingham, and S. M. Griffies, 2022: Kinetic energy transfers between mesoscale and submesoscale motions in the open ocean's upper layers. *Journal of Physical Oceanography*, **52 (1)**, 75–97, doi:10.1175/JPO-D-21-0099.1.

Pearson, B. C., J. L. Pearson, and B. Fox-Kemper, 2021: Advective structure functions in anisotropic two-dimensional turbulence. *Journal of Fluid Mechanics*, **916**, A49, doi:10.1017/jfm.2021.247.

Pearson, J., B. Fox-Kemper, R. Barkan, J. Choi, A. Bracco, and J. C. McWilliams, 2019: Impacts of convergence on structure functions from surface drifters in the Gulf of Mexico. *Journal of Physical Oceanography*, **49 (3)**, 675–690, doi:https://doi.org/10.1175/JPO-D-18-0029.1.

Pearson, J., and Coauthors, 2020: Biases in structure functions from observations of submesoscale flows. *Journal of Geophysical Research: Oceans*, **125 (6)**, e2019JC015 769, doi:https://doi.org/10.1029/2019JC015769.

Poje, A. C., T. M. Özgökmen, D. J. Bogucki, and A. Kirwan, 2017: Evidence of a forward energy cascade and kolmogorov self-similarity in submesoscale ocean surface drifter observations. *Physics of Fluids*, **29 (2)**, doi:https://doi.org/10.1063/1.4974331.

Qiu, B., T. Nakano, S. Chen, and P. Klein, 2022: Bi-Directional Energy Cascades in the Pacific Ocean From Equator to Subarctic Gyre. *Geophysical Research Letters*, **49 (8)**, e2022GL097 713, doi:10.1029/2022GL097713.

Renault, L., J. C. McWilliams, and J. Gula, 2018: Dampening of submesoscale currents by air-sea stress coupling in the Californian upwelling system. *Scientific reports*, **8 (1)**, 13 388, doi:https://doi.org/10.1038/s41598-018-31602-3.

Ross, A., Z. Li, P. Perezhogin, C. Fernandez-Granda, and L. Zanna, 2023: Benchmarking of Machine Learning Ocean Subgrid Parameterizations in an Idealized Model. *Journal of Advances in Modeling Earth Systems*, **15 (1)**, e2022MS003 258, doi:https://doi.org/10.1029/2022MS003258.

Sasaki, H., P. Klein, Y. Sasai, and B. Qiu, 2017: Regionality and seasonality of submesoscale and mesoscale turbulence in the north pacific ocean. *Ocean Dynamics*, **67**, 1195–1216, doi:https://doi.org/10.1007/s10236-017-1083-y.

Schubert, R., J. Gula, R. J. Greatbatch, B. Baschek, and A. Biastoch, 2020: The Submesoscale Kinetic Energy Cascade: Mesoscale Absorption of Submesoscale Mixed Layer Eddies and Frontal Downscale Fluxes. *Journal of Physical Oceanography*, **50 (9)**, 2573 – 2589, doi:https://doi.org/10.1175/JPO-D-19-0311.1.

Schubert, R., O. Vergara, and J. Gula, 2023: The open ocean kinetic energy cascade is strongest in late winter and spring. *Communications Earth & Environment*, **4 (1)**, 450, doi:https://doi.org/10.1038/s43247-023-01111-x.

Scott, R. B., and F. Wang, 2005: Direct Evidence of an Oceanic Inverse Kinetic Energy Cascade from Satellite Altimetry. *Journal of Physical Oceanography*, **35 (9)**, 1650 – 1666, doi:10.1175/JPO2771.1, URL https://journals.ametsoc.org/view/journals/phoc/35/9/jpo2771.1.xml.

Sheppard, K., and Coauthors, 2024: bashtage/arch: Release 7.0.0. Zenodo, URL https://doi.org/10.5281/zenodo.10981635, doi:10.5281/zenodo.10981635.

Spydell, M. S., F. Feddersen, and J. Macmahan, 2019: The effect of drifter GPS errors on estimates of submesoscale vorticity. *Journal of Atmospheric and Oceanic Technology*, **36 (11)**, 2101–2119, doi:10.1175/JTECH-D-19-0108.1.

Srinivasan, K., R. Barkan, and J. C. McWilliams, 2023: A Forward Energy Flux at Submesoscales Driven by Frontogenesis. *Journal of Physical Oceanography*, **53 (1)**, 87 – 305, doi:https://doi.org/10.1175/JPO-D-22-0001.1.

Steinberg, J. M., S. T. Cole, K. Drushka, and R. P. Abernathey, 2022: Seasonality of the Mesoscale Inverse Cascade as Inferred from Global Scale-Dependent Eddy Energy Observations. *Journal of Physical Oceanography*, **52 (8)**, 1677 – 1691, doi:10.1175/JPO-D-21-0269.1, URL https://journals.ametsoc.org/view/journals/phoc/52/8/JPO-D-21-0269.1.xml.

Storer, B. A., M. Buzzicotti, H. Khatri, S. M. Griffies, and H. Aluie, 2023: Global cascade of kinetic energy in the ocean and the atmospheric imprint. *Science Advances*, **9 (51)**, eadi7420, doi:10.1126/sciadv.adi7420.

Stroock, D. W., 2010: *Probability theory: an analytic view*. Cambridge university press.

Tedesco, P. F., L. E. Baker, A. C. N. Garabato, M. R. Mazloff, S. T. Gille, C. P. Caulfield, and A. Mashayek, 2024: Spatiotemporal Characteristics of the Near-Surface Turbulent Cascade

at the Submesoscale in the Drake Passage. *Journal of Physical Oceanography*, **54 (1)**, 187 – 215, doi:10.1175/JPO-D-23-0108.1, URL https://journals.ametsoc.org/view/journals/phoc/54/1/JPO-D-23-0108.1.xml.

Uchida, T., Q. Jamet, A. C. Poje, N. Wienders, W. K. Dewar, and B. Deremble, 2023: Wavelet-Based Wavenumber Spectral Estimate of Eddy Kinetic Energy: Idealized Quasi-Geostrophic Flow. *Journal of Advances in Modeling Earth Systems*, **15 (3)**, e2022MS003 399, doi:https://doi.org/10.1029/2022MS003399, URL https://agupubs.onlinelibrary.wiley.com/doi/abs/10.1029/2022MS003399, e2022MS003399 2022MS003399, https://agupubs.onlinelibrary.wiley.com/doi/pdf/10.1029/2022MS003399.

Vallis, G. K., 2017: *Atmospheric and oceanic fluid dynamics*. Cambridge University Press.

Wunsch, C., 1996: *The Ocean Circulation Inverse Problem*. Cambridge University Press, Cambridge, 437 pp.

Xie, J.-H., and O. Bühler, 2019: Third-order structure functions for isotropic turbulence with bidirectional energy transfer. *Journal of Fluid Mechanics*, **877**, R3, doi:10.1017/jfm.2019.651.

Yu, X., R. Barkan, and A. C. Naveira Garabato, 2024: Intensification of submesoscale frontogenesis and forward energy cascade driven by upper-ocean convergent flows. *Nature Communications*, **15 (1)**, 9214, doi:https://doi.org/10.1038/s41467-024-53551-4.

Zhang, Z., and Coauthors, 2023: Submesoscale inverse energy cascade enhances southern ocean eddy heat transport. *Nature Communications*, **14 (1)**, 1335, doi:https://doi.org/10.1038/s41467-023-36991-2.